Microstructure and mechanical properties of TC4/NiTi bionic gradient heterogeneous alloy prepared by multi-wire arc additive manufacturing

P.F. Jiang [a], M.H. Nie [a], X.M. Zong [b], X.B. Wang [c], Z.K. Chen [b], C.Z. Liu [d], J.Z. Teng [a], Z.H. Zhang [a,*]

[a] *Key Laboratory of Bionic Engineering, (Ministry of Education) and College of Biological and Agricultural Engineering, Jilin University, 5988 Renmin Street, Changchun, 130025, China*

[b] *State Key Laboratory of Intelligent Manufacturing of Advanced Construction Machinery, Xuzhou, 221004, China*

[c] *Key Laboratory for Liquid-Solid Structural Evolution and Processing of Materials (Ministry of Education), Shandong University, Jingshi Road 17923, Jinan, 250061, China*

[d] *Institute of Orthopaedic & Musculoskeletal Science, University College London, Royal National Orthopaedic Hospital, Stanmore, London, HA7 4LP, UK*

ABSTRACT

TC4/NiTi multi-materials structure components have been successfully fabricated via multi-wire arc additive manufacturing (MWAAM). Here we show the interface characteristics and mechanical properties of TC4/NiTi multi-materials structure component under bionic gradient interlayer build strategy. The results indicated that MWAAM TC4/NiTi gradient heterogeneous alloy with ultimate compression strength (1533.33 ± 26 MPa) was obtained. The excellent compression behaviour was mainly contributed to the excellent transition of gradient region indicated by EBSD analysis showing fine grain sizes and smaller difference Schmidt factor values. The phase composition from TC4 region to NiTi region had evolved with the increasing of NiTi content as follows: α-Ti + β-Ti → α-Ti + $NiTi_2$ → $NiTi_2$ → $NiTi_2$ + NiTi → NiTi + Ni_3Ti. The microhardness of the gradient het- erogeneous alloy ranged from 310 ± 8 HV to 230 ± 11 HV, and the highest hardness value was 669.6 ± 12 HV in region B due to the precipitation of $NiTi_2$ strengthening phase. The ultimate fracture stress and strain of sample were 1533.33 ± 26 MPa and 28.3 ± 6% respectively. The irrecoverable strain of MWAAM TC4/NiTi gradient heterogeneous alloy gradually approached 2.75% during 10 load/unload cycles of compression test.

1. Introduction

Ti6Al4V titanium alloys (TC4) have high specific strength and excellent fatigue resistance properties, and NiTi shape memory alloys have the advantages of shape memory effect (SME), superelasticity (SE) and high damping properties [1–4]. The characteristics of the two alloys have attracted much attention in aerospace components, bionic intelligent devices and weapon equipment systems and other advanced applications. However, some special components in the field of aerospace and nuclear energy are required to have excellent oxidation resistance, toughness, wear resistance and other properties, as well as high specific strength [5,6]. Such special requirements are often not available in traditional single TC4 alloy or NiTi alloy material structures. The multi-materials structure can combine the excellent properties of various alloy materials such as TC4 alloy and NiTi alloy, which can effectively reduce the weight of the alloy component and improve the strength and deformation properties of TC4/NiTi material in extreme environment. The development of TC4/NiTi multi-materials structural components will help to improve the thrust weight ratio and energy absorption and vibration resistance of space vehicles, thus promoting the rapid development of space industry [7].

Traditional metal multi-materials components are usually manufactured by brazing, friction stir welding, diffusion welding and other manufacturing methods [8–10]. These traditional methods are often limited by manufacturing methods, flexibility and high efficiency, and it is difficult to directly manufacture large-scale functional devices with TC4/NiTi multi-materials structure. Multi-wire arc additive manufacturing (MWAAM) technology is a kind of wire feeding metal additive manufacturing technology, which has the advantages of high deposition efficiency, material utilization rate, short manufacturing cycle, low manufacturing cost and large forming size range, etc [11–13]. It not only has great advantages in the manufacturing of large

* Corresponding author.
E-mail address: zhzh@jlu.edu.cn (Z.H. Zhang).

mechanical parts, but also can realize the integrated additive manufacturing of metal multi-materials components by controlling the feed speed of different metal wires to adjust the composition of materials.

However, NiTi alloys as an intermetallic compound have poor weldability. Moreover, the bonding strength between TC4 alloy and NiTi alloy will be reduced due to the formation of brittle phases in the process of directly preparing the metal multi-material structure of TC4 alloy and NiTi alloy [9,14]. On the other hand, the linear expansion coefficients of titanium alloy and NiTi alloy are quite different [15,16]. The phenomenon of fracture usually occurs when the internal stresses exceeds the yield strength of material in the process of direct welding and manufacturing of titanium alloy/NiTi alloy bimetallic structures [17]. These problems greatly limit the development of NiTi alloys in the design, manufacture and application of metal multi-materials structures.

In order to better adapt to the living environment, natural organisms have evolved multi-materials biological structures with multi-functional optimization and integration, such as bones, shells, shark skin, insect wings and so on [18,19]. Biological materials use different gradient configurations to achieve functional conversion to enhance certain mechanical functions, such as impact resistance, wear resistance, damage tolerance and toughness [20,21]. The multi-materials gradient configuration in biomaterials provides a large number of natural templates for the design of metal multi-materials integrated additive manufacturing [22–25]. The bionic gradient structure as the transition layer is helpful to reduce the difference of the linear expansion coefficient of the direct combination of dissimilar metals and reduce the internal stress generated during manufacturing, which is conducive to the suppression of the formation of cracks. It is expected to realize the integrated manufacturing of titanium/NiTi multi-materials metal parts.

Compositional gradient structure, as one of bionic structure, has attracted considerable academic attention owing to its application in the connection of heterogeneous metals fabricated additive manufacturing. Carroll et al. [26] investigated the influence of refractory metal monocarbide on microstructure and hardness of directed energy deposition SS304L/Inconel 625 functionally graded material. They demonstrated the feasibility of fabricating graded components by directed energy deposition and realized the thermodynamic calculations of the stability of a refractory metal monocarbide. Ma et al. [27] analyzed the microstructure and tensile properties of laser melting deposition functionally graded material TC4/TiAl. They claimed that the gradient structure effectively reduced the difference of thermal expansion coefficient between two metals. Moreover, the crack sensitivity was reduced resulting in the ideal metallurgical bonding in the whole alloy component was obtained. Han et al. [28] reported the phase evolution and mechanical properties of dual arc additive manufacturing TC4/Inconel 625 functionally graded material. They concluded that the element distribution of component had a good linear relationship with the increase of component height and the average ultimate compressive strength of vertical compression sample was 1390.25 MPa. Xu et al. [29] prepared 316L/TC4 functionally graded materials by directed energy deposition. This study showed that the FeTi based intermetallic compounds decreased with the increasing of content of TC4 powders. Meanwhile, the higher cooling rate induced by gradient laser powder can increase the growth restriction factor, and had greater undercooling ability to refine grains. Wang et al. [30] carried out a detailed study on the grain morphology of TA15/TC11 graded structural material obtained via wire arc additive manufacturing (WAAM), in particular, they mainly reported the change of mechanical properties with variation of deposition direction. They proposed that the performance of the transverse tensile gradient specimen was better than that of the specimen parallel to the building direction. Wang et al. [31] investigated the microstructure and corrosion property of plasma arc additive manufacturing Inconel 625/Cu functionally graded materials. They concluded that the equiaxed grains in the gradient sample increased with the increasing of Cu content due to that the addition of high growth restriction factor Q of Cu resulting in the increase the constitutional supercooling zone. In addition, they also reported that the Inconel 625/Cu materials had high ductility and excellent corrosion resistance which the hardness changed smoothly with composition changed.

Based on the above discussion, it is noticed that the studies on microstructure and mechanical properties of functional gradient materials for titanium alloy/stainless steel and titanium alloy/nickel-based alloys are already available in the literature. No previous publication has demonstrated a TC4/NiTi multi-materials structure entirely manufactured by MWAAM technology. Additive manufacturing of TC4/NiTi multi-materials structure components posed many challenges due to the significant differences in their material properties. No previous literature has been found to study bonding characteristics of TC4/NiTi interface fabricated via MWAAM. This study successfully fabricated a TC4/NiTi multi-materials structure containing bionic gradient heterogeneous interlayers by MWAAM. The different regions elements distribution, phase composition, crystallographic and microstructure evolution of TC4/NiTi gradient heterogeneous alloy were characterized, and the corresponding mechanical properties were discussed, aiming at studying the evolution of phase from TC4 to NiTi during the MWAAM process and discussing the effects of different phase on the microhardness, bending property and compression behavior. This research has taken the first step of WAAM TC4/NiTi multi-materials structure for aviation applications.

2. Experimental process

2.1. Materials and MWAAM process

In this experiment, the substrate is TC4 alloy plate of 150 mm × 150 mm × 5 mm TC4 and NiTi alloy wires with a diameter of 1.2 mm were used as raw materials. The nominal chemical compositions of the TC4 and NiTi alloy wires is shown in Table 1. The MWAAM system consists of a 6-axis ABB robot arm with a IRC5 controller, a shielding gas unit and wire feeders. The schematic of MWAAM system as shown in Fig. 1a. During this deposition process, only two wire feeders were used. The process of MWAAM was shown in Fig. 1b. The MWAAM environment was in the enclosed atmosphere with 99.99% purity argon. The more detail of other fundamental modules of the MWAAM can be found in previous work [24]. The MWAAM equipment used in this experiment was shown in Fig. 1c. The TC4/NiTi gradient heterogeneous alloy component with dimensions of 80 × 10 × 25 mm^3 from TC4 to NiTi was deposited on TC4 substrate by MWAAM. The TC4/NiTi gradient heterogeneous alloy component consists of three parts: TC4 alloy region, NiTi alloy region and gradient transition region. The gradient transition of material composition during MWAAM was obtained by controlling the wire feeding speed of two wires. The optimized process parameters during deposition were provided in Table 2. The schematics of the MWAAM TC4/NiTi gradient heterogeneous alloy component were shown in Fig. 1d–f.

2.2. Microstructure and crystallographic characterization

The sample after MWAAM was separated from the substrate by wire cutting and polished with sandpaper. To observe the evolution of microstructure in the TC4/NiTi gradient heterogeneous alloy component, the scanning electron microscopy (SEM, JSM-IT500A, Voltage: 10 kV, Current: 40 mA, Work distance: 11.5 mm) and the energy-dispersive X-ray spectrometer (EDS, JSM-IT500A) were used to characterize the microstructure and element distribution of the alloy materials. A D/Max 2500 PC X-ray diffractometer (XRD) with Cu Kα radiation was employed to determine the phase constituents of the samples processed with different regions. Electron backscatter diffraction (EBSD) was used to investigate the grain orientation and grain boundary misorientation in the cross section of the MWAAM samples. A step size of 0.8 μm was selected to observe the morphology of grains. The EBSD data were post-

Table 1
The nominal chemical compositions of the TC4 and NiTi alloy wires.

	Al	V	Co	Cu	Cr	Nb	Ni	Fe	C	N	O	Ti
TC4	6.20	4.02	–	–	–	–	–	0.02	0.01	0.01	0.09	Bal.
NiTi		–	0.005	0.005	0.005	0.025	55.85	0.005	0.032	0.001	0.039	Bal.

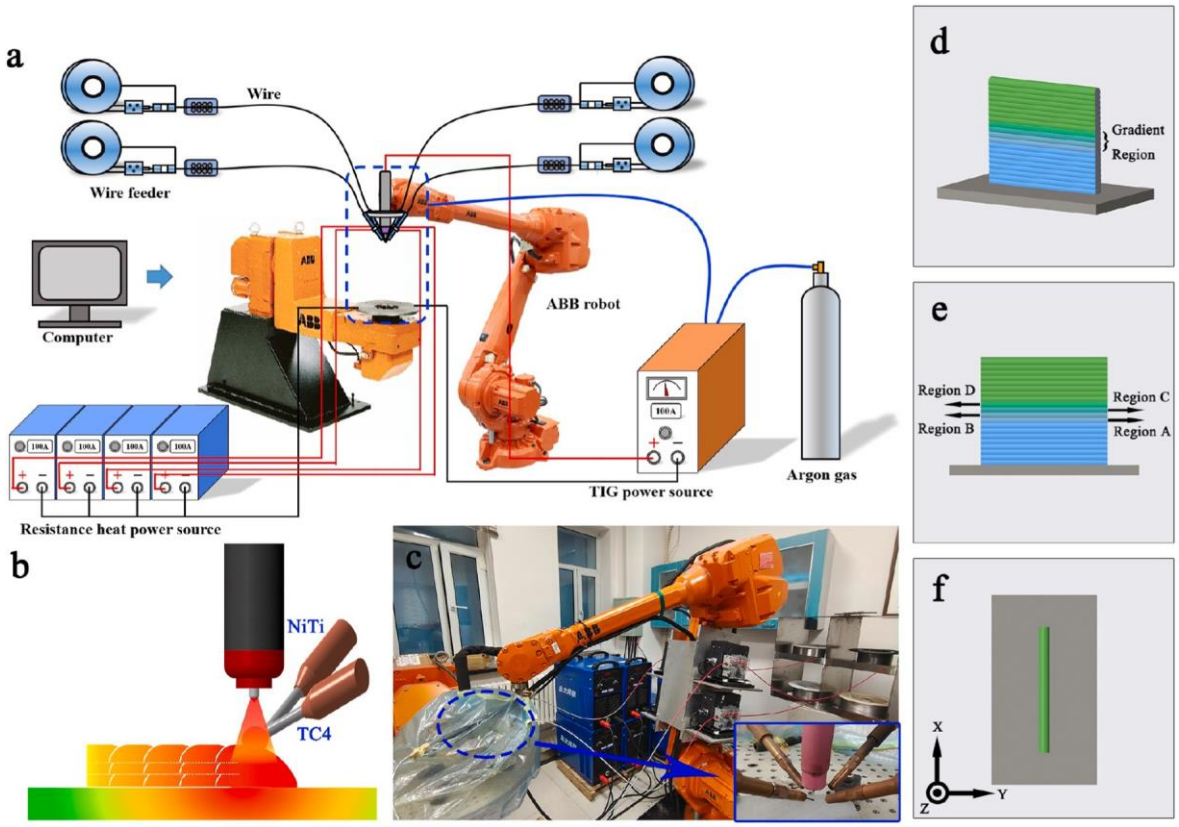

Fig. 1. (a) Schematic of the MWAAM system; (b) Working principle of two wires arc additive manufacturing process; (c) Photograph of the MWAAM equipment; (d–f) Diagram of different angle of an as-built component.

Table 2
The optimized MWAAM process parameters about this experiment.

Region	Peak current (A)	Base current (A)	TC4 mwire feed velocity (cm/min)	NiTi wire feed velocity (cm/min)	TC4 hot-wire current (A)	NiTi hot-wire current (A)	Moving speed (mm/min)	Shielding gas flow rate (L/min)
TC4	200	9	130	–	100	–	300	20
Reigion A	220	9	90	40	100	120	300	20
Reigion B	220	9	50	80	100	120	300	20
Reigion C	220	9	80	50	100	120	300	20
Reigion D	220	9	40	90	100	120	300	20
NiTi	220	9	0	130	–	100	300	20

processed with HKL Channel 5 analysis software.

2.3. Mechanical properties and fracture analysis

The microhardness of cross-section (Y-Z plane) of samples was performed using a Vickers automatic hardness tester (Huayin, HVS-1000), with a test load of 200 g and dwell time of 15 s. Each position for three times to take the average value to reduce the error. The hardness indentation morphology was observed via optical microscopy (OM, ZEISS-Scope AI). Compression tests (single and cyclic) were performed using a compression tester (Instron 1121) to evaluate the mechanical properties of the components. The size of compression specimens was Φ 4 mm × 8 mm. The loading rate were 1 mm/min and 0.5 mm/min for single and cyclic compression tests respectively. The three-point bending test was carried out by universal tester (Instron 1121), in which the span was 10 mm and the loading rate was 0.5 mm/min. The size of bending specimens was 22 mm × 4 mm × 2 mm. Three repetitions compression test and three-point bending test were carried out under the same testing conditions to acquire an average value. The fracture surface of the samples after compression and bending test was

observed by SEM to evaluate the failure mechanisms.

3. Results and discussion

3.1. Morphological and EDS mapping characteristics of TC4 to NiTi samples interfaces

The bonding state between different metal deposition layers had an important influence on the overall performance of alloy components. To observe the microstructure evolution and interface transition between different gradient layers, SEM observation and EDS measurement was conducted for all interfaces. The interface microstructure of TC4/NiTi gradient heterogeneous alloy is shown in Fig. 2. It can be seen from Fig. 2a–d that good metallurgical bonding had taken place at the interface between different alloy gradient regions, and no fusion defects such as pores and cracks had been found. From the microstructure morphology of gradient alloy components, it can be seen that there were five interfaces and six regions formed during the transition from TC4 to NiTi alloy. The four regions of the gradient part from TC4 to NiTi were named as region A, region B, region C and region D, respectively. The region of TC4 alloy was mainly composed of α-Ti and β-Ti, which was typical basket-weave structure. With the increase of NiTi content in the molten pool, the dual phase structure of TC4 changed at the interface. It can be seen from Fig. 2a that the proportion of the lamellar primary α phase structure near theTC4 alloy side tends to decrease gradually. Since nickel element was a eutectoid β stable element, adding nickel element to titanium alloy can reduce the β transition temperature and enlarge the β phase region. Therefore, the proportion of β phase increased at the interface near TC4 alloy side. However, the microstructure morphology had changed greatly at the interface near region A side. The typical basket-weave structure of TC4 alloy was transformed into white massive eutectic structure, as shown in Fig. 2b. With the further increase of NiTi content, the white massive eutectic structure transformed into irregular strip structure, as shown in Fig. 2b. Compared with region B, the microstructure morphology of region C changed into grid structure. When the proportion of NiTi in the molten pool was high, the microstructure of black grid structure in region C gradually decomposed to a discontinuous sphere structure, thus forming region D, as shown in Fig. 2c. However, the black spherical structure disappears completely when only NiTi wire melt dropped into the molten pool, which was a typical NiTi alloy structure, as shown in Fig. 2d. Through the analysis of the microstructure and morphology of each deposition gradient layer, it can be seen that the integrated MWAAM of TC4/NiTi gradient heterogeneous alloy can be realized by using the bionic gradient structure.

A larger diffusion distance of dissimilar metal elements is helpful to enhance the metallurgical bonding strength of dissimilar materials [32]. In order to further analyze the bonding state between different gradient layers of TC4/NiTi gradient heterogeneous alloy, EDS line scanning analysis was performed on all interfaces. The EDS diagram at the interface of TC4/NiTi gradient heterogeneous alloy materials is shown in Fig. 3. It was noted that a narrow interdiffusion zone was formed at the interface. A certain degree of diffusion of all elements in interdiffusion zone can be observed from TC4 to the region A, as shown in Fig. 3a. However, the diffusion degree of nickel element was smaller than that of Al and V elements, indicating that this element had no mix strongly at this interface. The clear interface further proved this point. Tang et al. [33] studied the element diffusion behavior of CMT nickel-based and iron-based coatings, they found that the elements with higher concentration in the coating were difficult to diffuse into the matrix. A similar phenomenon was found when region A was deposited on TC4 matrix. This may be due to the relatively low diffusion coefficient of Ni on the TC4 side. According to Fick's first law, the higher the

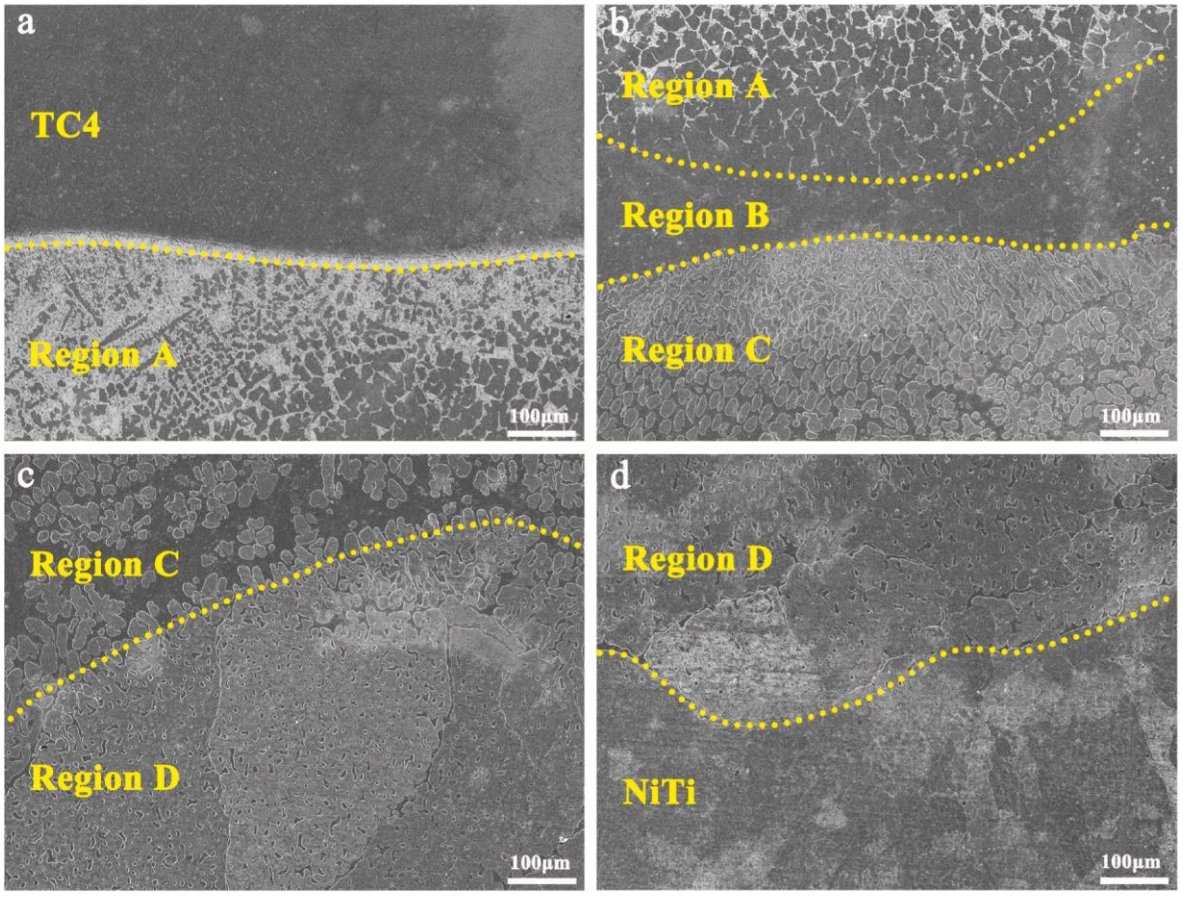

Fig. 2. SEM microstructure (Y-Z plane) of MWAAM TC4/NiTi gradient heterogeneous alloy from TC4 to NiTi region.

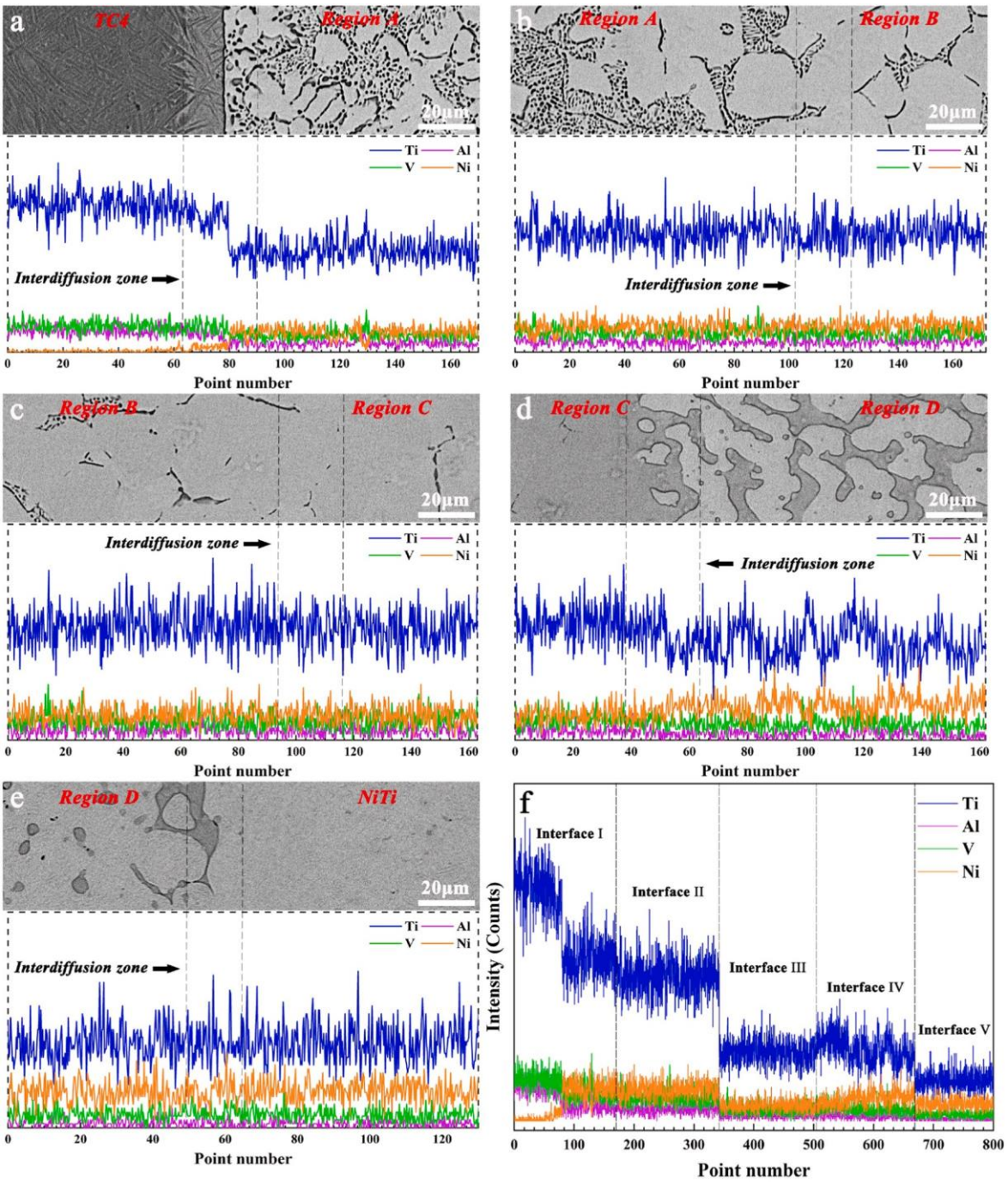

Fig. 3. Line scanning of elements near the interface: (a) Interface I; (b) Interface II; (c) Interface III; (d) Interface IV; (e) Interface V; (f) Interface I–V.

diffusion coefficient, the greater the elemental flux [34]. Therefore, the content of Ni element diffused to TC4 side was relatively small. In addition, some of the Ni elements may have evaporated (The boiling point: Ni 2913 °C, Ti 3287 °C) due to excessive heat input during the simultaneous feeding of the double wires into the molten pool, resulting in a reduction in the amount of Ni element diffused to the TC4 side. The EDS element curve of the interface between region A and region D had huge fluctuation, which meant that the elements on these two sides were strongly mixed with a high degree of mixing, as shown in Fig. 3b–d. This indicated that the two adjacent regions had achieved good metallurgical combination. It was worth noting that, as shown in Fig. 3e, there was almost no Al signal in the entire EDS line scanning area. The reason for this phenomenon was that the proportion of Al content sent into the molten pool was small in the fourth gradient layer. On the other hand, the melting point of Al element was low, so it was easy to burn out in the deposition process, resulting in a certain degree of content loss. Fig. 3f is an integration of intensity line scanning distribution of all interface elements to observe the rough distribution process of elements. It can be seen from Fig. 3f that the overall strength of Ti element decreased in a stepwise manner, indicating that there was a compositional transition zone between TC4 alloy and NiTi alloy. Based on the above experimental results, it could be concluded that TC4/NiTi gradient heterogeneous alloy manufactured by MWAAM technology had good metallurgical combination and microstructure stability.

3.2. Morphology and distribution of intermetallic phase

In order to determine the phase composition of the different regions and the phase evolution process of the TC4/NiTi gradient heterogeneous alloy, the XRD detection of the six regions was carried out, and the results are shown in Fig. 4a. TC4 alloy was mainly composed of α-Ti and β-Ti phases. The phase structure of MWAAM TC4 alloy had been studied in detail in previous reports [35]. With the increase of NiTi wire feeding speed, β-Ti phase changed to $NiTi_2$ phase. The phase diagram of Ni–Ti system is shown in Fig. 4b. When the content of Ni element in the molten pool was small, β-Ti was firstly precipitated during the cooling process, and the reaction was L→β-Ti. When the eutectic line was reached with the further decrease of the temperature, the eutectic reaction will occur and $NiTi_2$ will appear in the liquid phase as L→β-Ti + $NiTi_2$. When the temperature was between the eutectic line and eutectoid line, part of β-Ti changed to $NiTi_2$. When the temperature dropped to the eutectoid line, α-Ti and $NiTi_2$ were formed by the eutectoid reaction of β-Ti→α-Ti + $NiTi_2$. Since the cooling rate of WAAM process ($10–10^{2}$°C) was relatively slower than that of laser AM process ($10^{3}–10^{4}$°C [36]), β-Ti phase had a longer time to transform into α-Ti and $NiTi_2$ phases. In addition, the window of the non-stoichiometric composition space of NiTi at high temperature was relatively narrow due to the presence of $NiTi_2$ and Ni_3Ti phases on both sides of NiTi phase. Therefore, the non-equilibrium solidification process may lead to compositional segregation and induce the formation of $NiTi_2$ or Ni_3Ti. With the further increase of Ni content, NiTi phase formed in regions B, C and D. All three regions were composed of $NiTi_2$ and NiTi phases. The difference was that the peak intensity of NiTi gradually increased with the increase of Ni content, indicating that the NiTi phase in the region was gradually increased. In the pure NiTi region, a small amount of precipitated $NiTi_2$ and Ni_3Ti were also found in addition to NiTi phase. Jian Han et al. [37] reported that the metastable phases of Ni_4Ti_3 and Ni_3Ti_2 could be observed in the early stage of low-temperature aging period of WAAM NiTi process. However, in the process of layer by layer accumulation of heat input, the previously deposited layer was considered to be undergoing in situ aging, and Ni_4Ti_3 and Ni_3Ti_2 gradually decomposed into Ni_3Ti phase. The reaction was Ni_4Ti_3→ Ni_3Ti_2 → Ni_3Ti. The similar phenomenon was found in this paper.

In order to establish the relationship between phase and microstructure of TC4/NiTi gradient heterogeneous alloys, high magnification SEM of microstructure and EDS measurement were carried out in different gradient regions. The microstructure images of TC4, NiTi and the four gradient regions are shown in Fig. 5. Table 3 lists the EDS results at different points in Fig. 5. Fig. 5a shows the microstructure of TC4 alloy, which was mainly acicular net structure. Fig. 5b shows the microstructure of region A. Since the substrate of region A was TC4, the surface of TC4 remelted during the deposition of region A, resulting in a relatively high Ti content and a relatively low volume fraction of NiTi in the molten pool. Combined with EDS results, it can be seen that the eutectic region in region A was α-Ti + $NiTi_2$, and the black bulk region was mainly $NiTi_2$. The Gibbs free energies of formation of the $NiTi_2$ phase and NiTi are —74.7 kJ/mol and —58.2 kJ/mol [38]. According to the Gibbs free energy of two-phase formation, $NiTi_2$ was preferentially precipitated. With the increase of Ni content, α-Ti in region B gradually disappeared and a large area of $NiTi_2$ phase was formed, as shown in Fig. 5c. After EDS measurement of the microstructure of regions C and D, it was found that regions C and D formed a bi-phase region consisting of NiTi and $NiTi_2$. It was note that the Ni content in region C was less than that in region D. The microstructure of region C and D is shown in Fig. 5d and e. In region C, $NiTi_2$ and NiTi dual phase structures with network $NiTi_2$ as the matrix were formed. In region D, the $NiTi_2$ and NiTi dual phase structures with spherical $NiTi_2$ as precipitated phases were formed. The NiTi region was mainly columnar crystal, as shown in Fig. 5f. It was worth noting that precipitates of different sizes were observed at the grain boundaries and inside the columnar crystals. The results of EDS and XRD showed that the precipitated phase was Ni_3Ti. Yulin et al. [39] reported that the existence of grain boundaries and the supersaturation of Ni will affect the nucleation of Ni_4Ti_3, and metastable Ni_4Ti_3 can be decomposed into Ni_3Ti precipitates. In the case of MWAAM, Marangoni convection effect led to nickel element segregation and local supersaturation, which promoted the nucleation of Ni_4Ti_3 precipitation and then decomposed to produce Ni_3Ti phase. In addition, the high interface energy at the grain boundary promoted the preferential nucleation and growth of Ni_3Ti [37]. Therefore, Ni_3Ti at the grain boundary was mainly needle shaped, while Ni_3Ti in grains was mostly granular.

Fig. 6 demonstrates the microstructure evolution of the TC4/NiTi gradient heterogeneous alloy in details under different gradient regions. TC4 titanium alloy was a cross acicular dual phase structure. With the increase of Ni content in the deposition process, the eutectic reaction of Ti and Ni occurred, and the eutectic structure of α-Ti and $NiTi_2$ was formed, as shown in region A. Then, the proportion of $NiTi_2$ phase increased gradually until it occupied the entire matrix (Region B). The NiTi phase formed when the Ni content of the deposition layer exceeded 34 wt% [37]. At the third gradient layer (Region C) of the alloy, blocky NiTi phase was formed on $NiTi_2$ matrix. With the further increase of Ni content, when reaching the fourth gradient layer (Region D), the proportion of NiTi phase further increased, and the morphology of $NiTi_2$ phase gradually dissolved from network to spherical, forming a structure dominated by NiTi phase. When reaching the pure NiTi region on the top

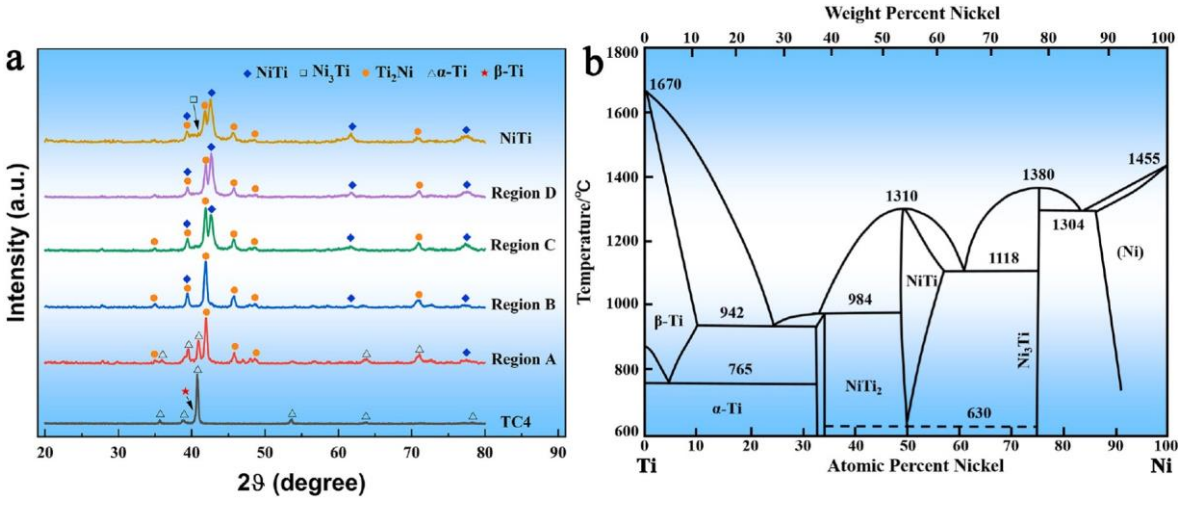

Fig. 4. (a) XRD patterns of MWAAM TC4/NiTi gradient heterogeneous samples at different regions; (b) Ti–Ni binary phase diagram.

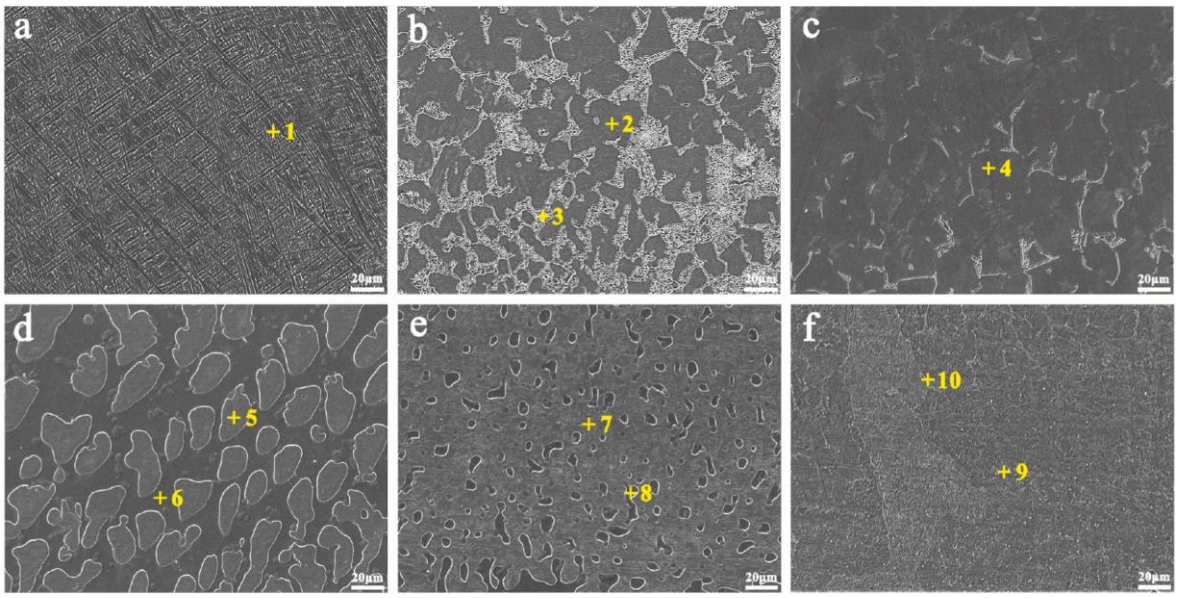

Fig. 5. The SEM microstructure (Y-Z plane) of different regions of MWAAM TC4/NiTi gradient heterogeneous alloy: (a) TC4 region; (b) Region A; (c) Region B; (d) Region C; (e) Region D; (f) NiTi region.

Table 3
EDS results of selected points in Fig. 5.

Position	Ti	Ni	Al	V	Possible phase
1	88.22	0.16	8.52	3.10	α-Ti + β-Ti
2	64.61	30.57	4.20	0.62	$NiTi_2$
3	80.47	8.01	7.42	4.10	α-Ti + $NiTi_2$
4	70.39	27.29	1.66	0.66	$NiTi_2$
5	52.51	46.25	1.24	–	NiTi
6	65.41	31.00	3.59	–	$NiTi_2$
7	52.04	47.09	0.87	–	NiTi
8	65.78	32.64	1.58	–	$NiTi_2$
9	51.94	48.06	–	–	NiTi
10	27.17	72.83	–	–	Ni_3Ti

of the alloy sample, the microstructure was typical NiTi phase structure. A small amount of Ni_3Ti precipitates were dispersed in NiTi phase structure due to the non-equilibrium solidification process with large heat input produced by WAAM. According to the phase diagram Fig. 4b, the microstructure evolution process of TC4/NiTi gradient heterogeneous alloy gradually changed with the change of Ni content, and the phase composition structure was consistent with the phase diagram analysis results. The microstructure and phase evolution process from TC4 to NiTi was α-Ti + β-Ti→α-Ti + $NiTi_2$→$NiTi_2$→$NiTi_2$+NiTi→NiTi + Ni_3Ti. Therefore, TC4 alloy and NiTi alloy can be manufactured by integral additive in the form of composition gradient transition by changing the wire feeding speed ratio of TC4 and NiTi wires.

3.3. Grain orientation and crystallographic texture

In order to further study the crystallographic characteristics of different regions of MWAAM TC4/NiTi gradient heterogeneous alloy, EBSD analysis was carried out, and the results are shown in Fig. 7. Firstly, the grain morphology and orientation of the top NiTi region and the bottom TC4 region of the gradient heterogeneous alloy sample were analyzed (along the building direction, Z-axis). From the top, the microstructure of NiTi alloy region prepared by MWAAM was mainly composed of coarse grains, as shown in Fig. 7a. In addition, most grains of NiTi alloy were red in the analysis, which indicated that the grains mainly grew along the direction of<001>. Meanwhile, it was known that NiTi grains had relatively strong texture (maximum projected polar density = 22.21) according to the inverse polar diagram (IPF) and polar diagram (PF) in Fig. 7b. In addition, a few blue and green particles were scattered on the surface representing<111>and<110>grain orientations, respectively. It is well known that temperature gradient (G) and solidification rate (R) during additive manufacturing process are important factors that affect grain orientation and solidified structure morphology [40]. Since the initial solidification driving force comes from the direction of the maximum temperature gradient, the <100> orientation parallel to the building direction is usually regarded as the most effective heat dissipation path, so the columnar grains of the cubic alloy grow preferentially along the <100> direction, resulting in a strong crystalline texture [41,42]. Fig. 7c is the statistical diagram of grain misorientation distribution of NiTi alloy. The low angle grain boundaries (LAGBs) are 2°–15°, and the high angle grain boundaries (HAGBs) are >15°, so as to distinguish the orientation angle of the alloy sample. The grain boundary type of NiTi sample was dominated by HAGBs, and the proportions of HAGB and LAGB were 62.5% and 37.5% respectively. Fig. 7d shows the EBSD observation results in TC4 region. It can be seen from Fig. 7d that the grain size of TC4 was relatively large. The results of IPF and PF showed that the texture density in TC4 region was relatively lower than NiTi region, as shown in Fig. 7e. In addition, the proportion of the HAGBs in TC4 region was 95.91%, and that of the LAGBs was only 4.09%, as shown in Fig. 7f. One of the reasons for this phenomenon was that a large number of α particles cross easily to form high angle grain boundaries [43]. On the other hand, the orientation difference between adjacent grains increased due to the decrease of texture strength, which resulted in the increase of the proportion of HAGBs [44].

Fig. 8 shows the EBSD grain orientation maps of the gradient region of the MWAAM TC4/NiTi gradient heterogeneous alloy, which will be used to investigate the formation mechanism of the gradient grain morphology around the interface. It can be seen that the grain structure. Fig. 8a shows that no preferred orientation from the grains in region A was formed. Fig. 8b shows grain-size distributions of region A that were concentrated at 0–5 μm, accounting for 88.88% of the total, while the total number of grains larger than 26 μm accounted for 3.3% of the total, with an average size of 3.389 μm. Fig. 8c and d shows orientation and grain size distribution results for region B, where the grain orientation was multi-axial (Fig. 8c). The maximum grain size was 69.35 μm, and sizes greater than 26 μm accounted for only 0.38%, with an average of

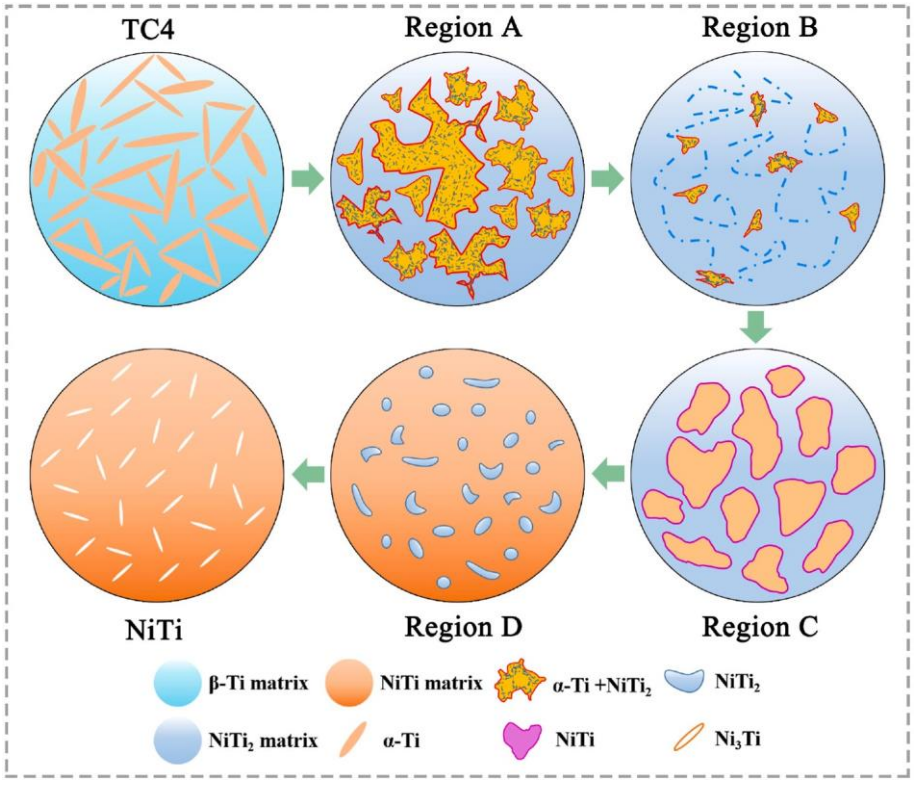

Fig. 6. Schematic diagram of microstructural evolution of MWAAM TC4/NiTi gradient heterogeneous alloy from TC4 to NiTi region.

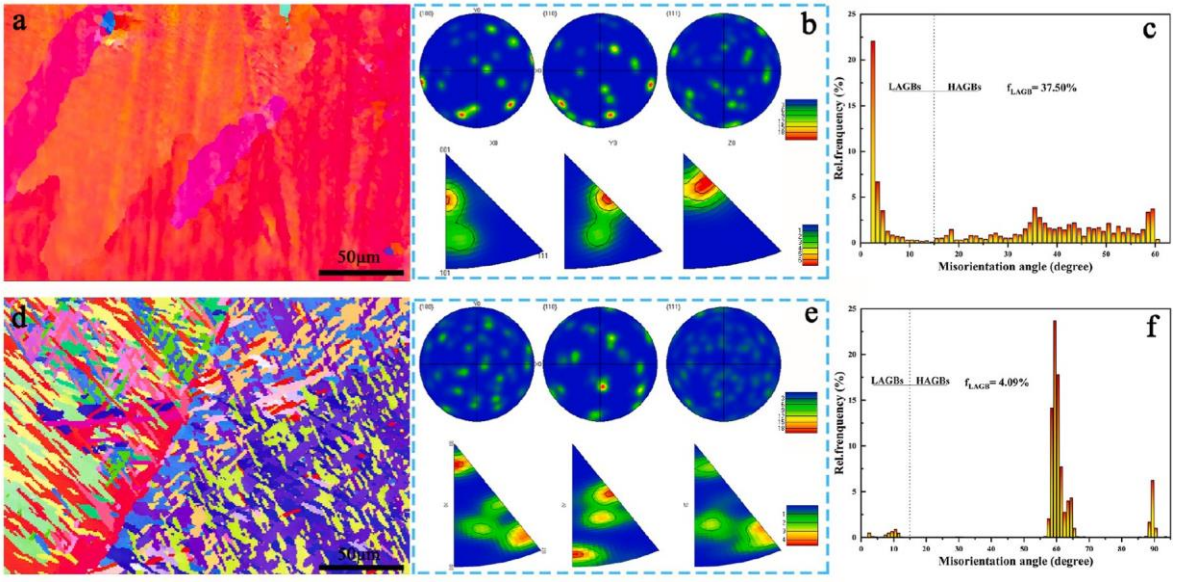

Fig. 7. IPF, PF maps and statistics charts of misorientation angle distributions of MWAAM TC4/NiTi gradient heterogeneous alloy determined by EBSD: (a–c) TC4 region; (d–f) NiTi region.

2.145 μm. Fig. 8e andf shows that the grain size for region C was reduced by 48.1%, relative to that for region A. Fig. 8g and h shows that the grain orientation region D was same as that for region C, mainly was random orientation. However, the grain size increased to an average of 2.047 μm, and grains larger than 26 μm accounted for 0.71% of the total with region D (Fig. 8h). This was slightly larger than that from region C (Fig. 8e).

The polar density of metal texture had a significant influence on its properties [45]. The mechanical properties of alloy material would appear anisotropic when the value of polar density was large. This was due to the fact that the sliding system of alloy would deform in a certain direction during plastic deformation process and the texture polar density would lead to different deformation difficulties in all directions resulting in the strength and plasticity of alloy materials different in all directions. The polar map of gradient region A-D corresponds to {100}, {110} and {111}, as shown in Fig. 9a–d. The texture in <001> direction was easy to be formed in the wire arc additive manufacturing process, which was consistent with the direction of the maximum cooling rate

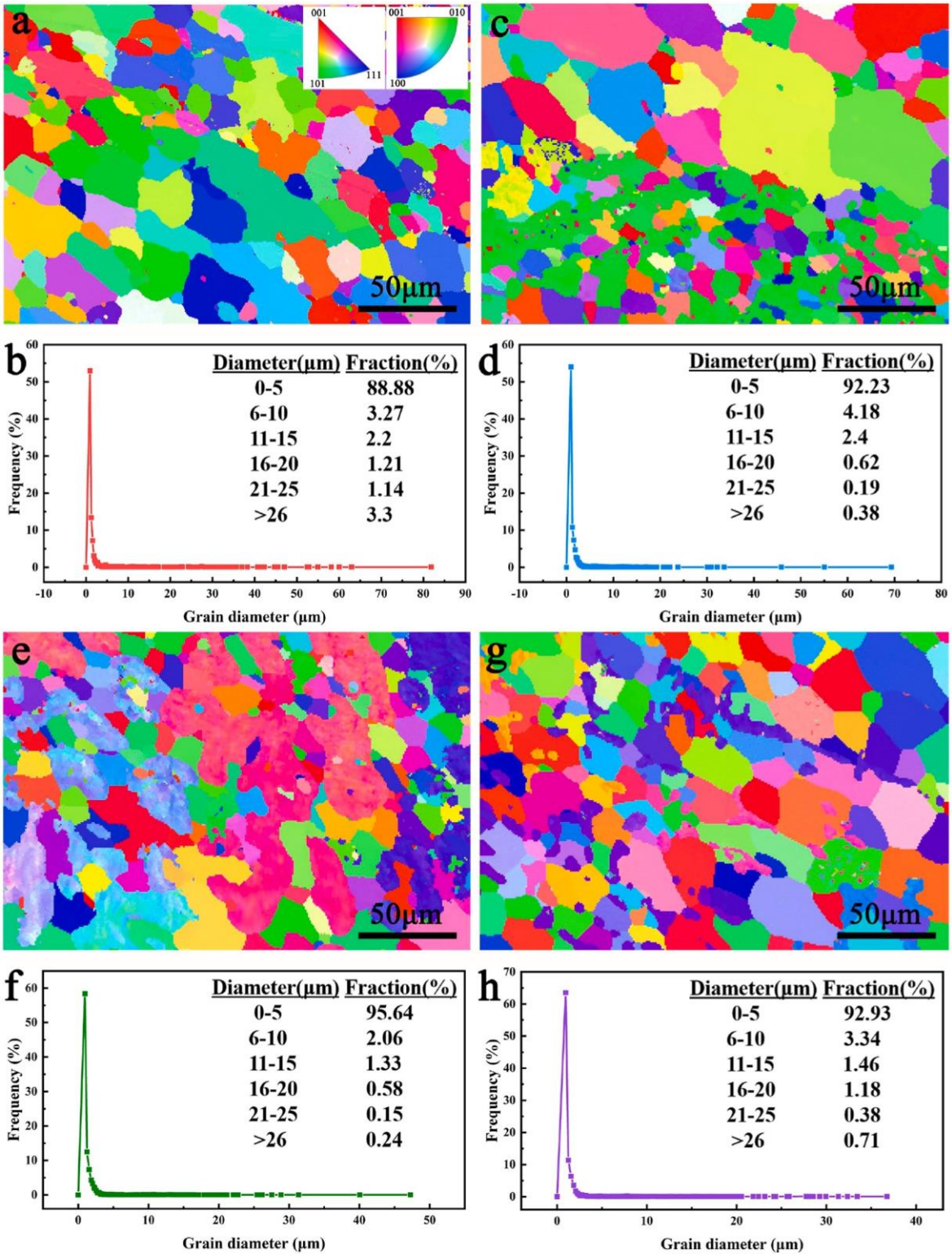

Fig. 8. EBSD results of MWAAM TC4/NiTi gradient heterogeneous alloy: (a, c, e, g) Grain morphology; (b, d, f, h) Proportion, and change trend of grain sizes for different region; (a–b) Region A; (c–d) Region B; (e–f) Region C; (g–h) Region D.

[46]. However, the texture caused by higher polar density was not found in the gradient region of TC4/NiTi gradient heterogeneous alloy. The polar density of region A-D was 4.16, 8.32, 4.63 and 4.20 respectively, which was significantly lower than TC4 and NiTi regions, indicating that the grain orientation of the four gradient regions was more random. Zhang et al. [47] believed that the lower influence range of high temperature and the larger thermal gradient had a higher selectivity to the grain growth direction, while the "texture dilution" effect provided by Burgers orientation relationship would weaken this directional solidification selectivity.

The slip of dislocations during metal deformation follows Schmidt's law, and the slip system with larger value is activated preferentially

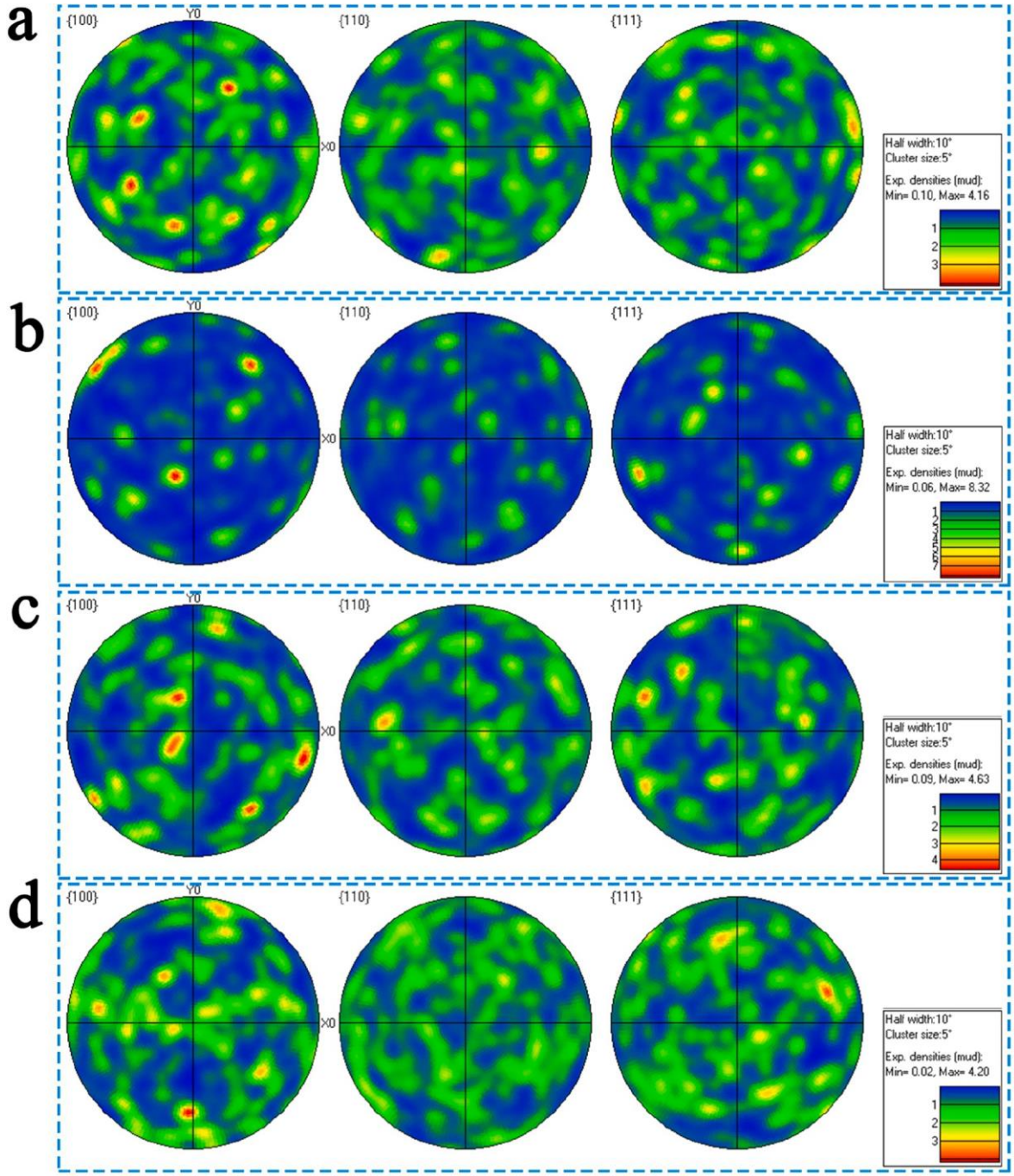

Fig. 9. Pole figures of MWAAM TC4/NiTi gradient heterogeneous alloy: (a) Region A; (b) Region B; (c) Region C; (d) Region D.

[48]. Cui et al. [40] believed that the increase of Schmidt factor value was beneficial to reduce the possibility of crack initiation caused by stress concentration, thus improving the ductility of alloy samples. Therefore, the Schmidt factor values corresponding to different regions of TC4/NiTi gradient heterogeneous alloys were analyzed. Fig. 10a–f shows the statistical results of the Schmidt factor on the sample surface in different regions. The corresponding entire Schmidt factor image was inserted into each statistic diagram. It can be seen that from TC4 to NiTi region, the Schmidt factor of the sample gradually increased, and the average Schmidt factor for six regions were 0.365, 0.445, 0.446, 0.450, 0.451 and 0.484, respectively. It was note that the red region with high Schmidt coefficient became more concentrated in NiTi region of sample. Therefore, it was reasonable to assume that the ductility of the material gradually improved with the transition from TC4 to NiTi. In addition, the difference between the Schmidt factor values of the gradient region A-D was small, indicating that the possibility of cracking between region A-D in the material gradient region was low. However, the difference between Schmidt factor values in TC4 and region A was large, as shown in Fig. 10f indicating that it was easier to crack here due to excessive performance difference [49].

3.4. Mechanical properties

The microhardness distribution diagram of TC4/NiTi gradient heterogeneous alloy along the building direction was shown in Fig. 11. The indentation topography corresponding to some positions was inserted into the microhardness distribution map. The average microhardness in TC4 region was about 310 ± 8 HV. The microhardness of region A-D in

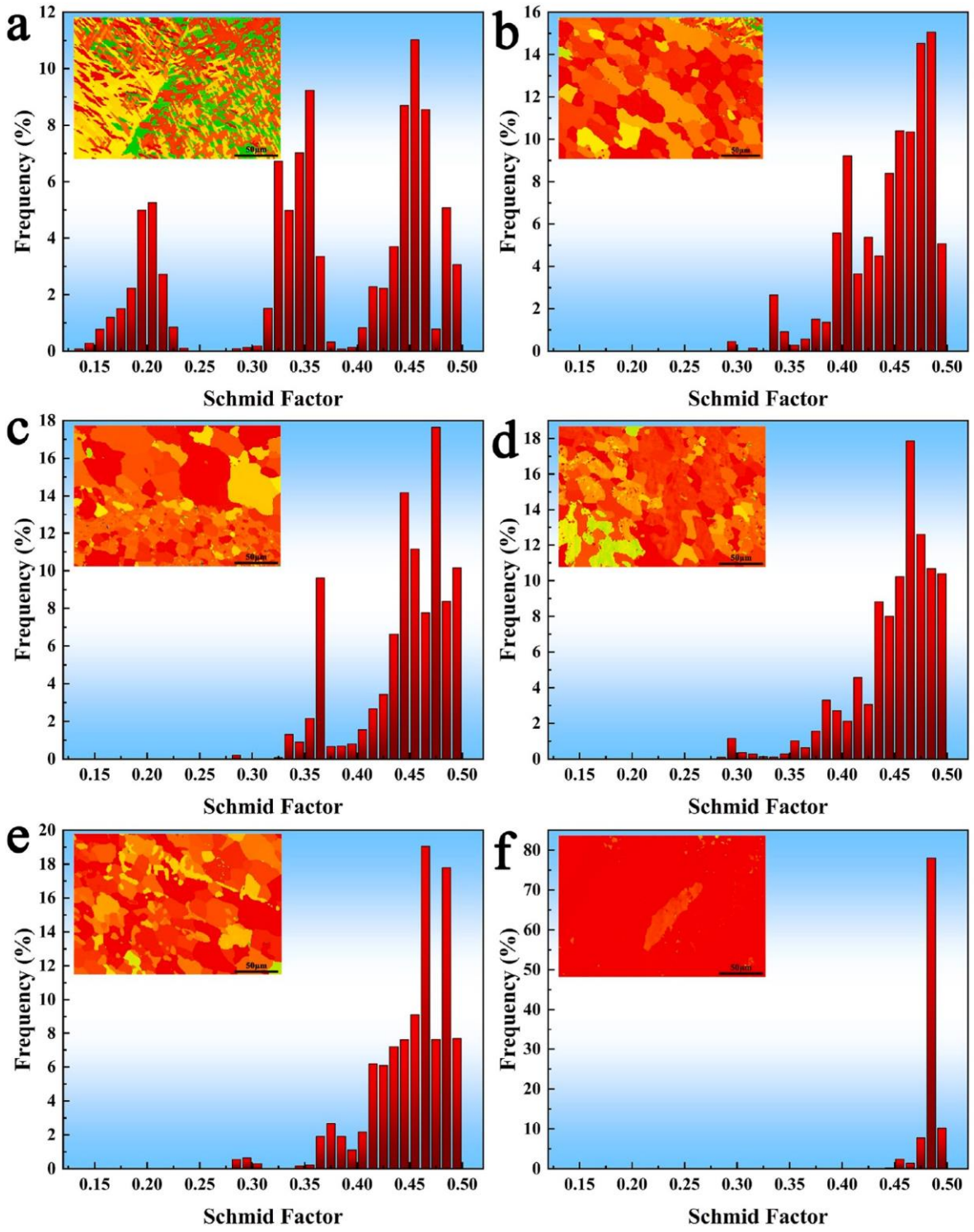

Fig. 10. Schmidt factor distribution of MWAAM TC4/NiTi gradient heterogeneous alloy: (a) TC4 region; (b) Region A; (c) Region B; (d) Region C; (e) Region D; (f) NiTi region.

the gradient region first increased and then decreased, and finally reached the NiTi region to be stable. The initial increase in hardness was due to that the large number of $NiTi_2$ phases formed in region A and B resulting from the high Ti content in TC4. The highest hardness value was 669.6 ± 12 HV, which was found in region B. It should be noted that cracks appeared due to the high hardness of $NiTi_2$ during the hardness test, as shown in the indentation photo of region B in Fig. 11. It can be seen from the above that region C was composed of NiTi and NiTi two-phase structures, and the average microhardness was 293.2 ± 22 HV. The phenomenon of $NiTi_2$ agglomeration observed in some areas, and its hardness reached 546.6 ± 8 HV, as shown in Fig. 11. The microhardness of region D decreased significantly compared with region A-C. The microhardness decrease of region D was attributed to the changed of its matrix from $NiTi_2$ to NiTi, resulting in the overall decrease of its hardness to 248.2 ± 24 HV. The average microhardness value of NiTi region was 230 ± 11 HV. The microstructure analysis showed that this region

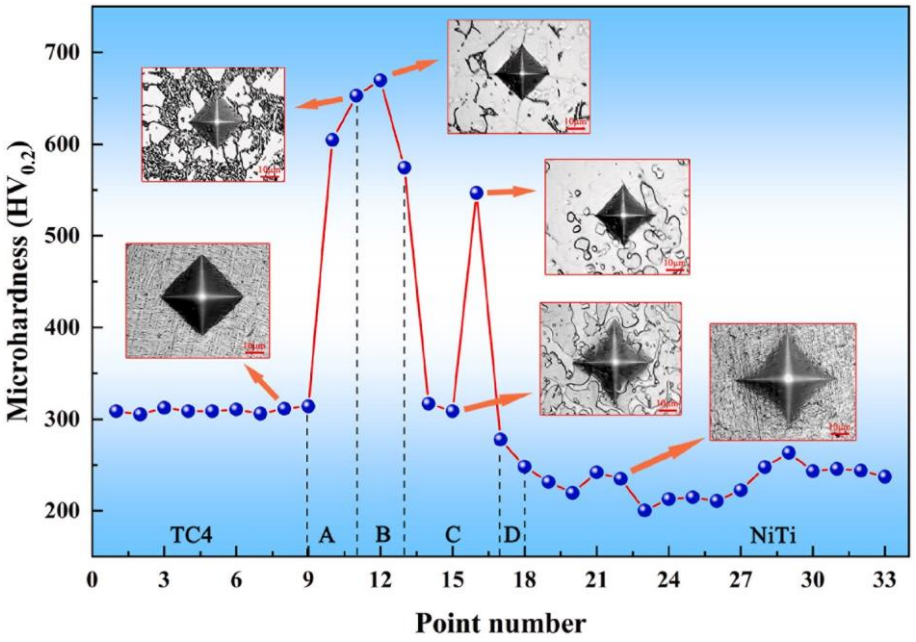

Fig. 11. Vickers hardness values of MWAAM TC4/NiTi gradient heterogeneous alloy.

was composed of NiTi matrix and a small amount of Ni_3Ti precipitate. The formation of Ni_3Ti precipitate had the pinning effect of preventing dislocation migration and improving material hardness [37]. In addition, the microhardness of NiTi region fluctuated slightly as shown in Fig. 11, which was related to the volume fraction of $NiTi_2$ precipitation. According to the above analysis, the microhardness of TC4/NiTi gradient heterogeneous alloy tended to increase first and then decrease. Note that the hardness between TC4 and region A had a large gap, and the microhardness from 310 ± 8 HV to 604.5 ± 14 HV, which might reduce the strength of the alloy sample and cause cracking. In order to further analyze the evolution of the interface between TC4 and region A, crystallographic tests were conducted through EBSD, the results as shown in Fig. 12. The orientation map of interface indicates that the grains grow perpendicular to the interface in the region A, showing an orientation of <001>. Meanwhile, no preferred orientation was observed in the TC4 region, as shown in Fig. 12a. Fig. 12b shows the phase distribution of the interface between TC4 and region A. The phase of α-Ti and $NiTi_2$ are shown in red and blue respectively. It can be seen that the TC4 region was mainly α-Ti phase while the region A was composed of $NiTi_2$ and α-Ti phase. The crystal structures of α-Ti and $NiTi_2$ phases were different, resulting in obvious boundary formed between two phases at the interface, as shown in Fig. 12b. In addition, the diffusion-like α-Ti phase was also formed in region A due to the interdiffusion of elements at the interface. Combining with Fig. 12c, smaller grains were found at the interface near TC4 region side, which was related to the refinement of grains due to the diffusion of Ni element. The kernel average misorientation (KAM) can reflect the degree of homogenization of plastic deformation of the alloy sample [50]. The degree of homogenization of plastic deformation usually affects the stress distribution. Therefore, it is necessary to analyze the KAM distribution map at the interface. The KAM map of the interface between TC4 and region A was presented by color bands ranging from 0 to 5°, as shown in Fig. 12d. The blue and red colors indicated the lowest and the highest value, respectively. KAM map in Fig. 12d shows that green is mainly distributed at grain boundary and interface, indicating high dislocation density and large plastic deformation at grain boundary and interface. This was due to the fact that the dislocations need more energy to migrate resulting in dislocation stacking when they moved to the grain boundary, and then the positions with large KAM values were mainly located at the grain boundary [47]. The same phenomenon happened at the interface. In addition, it can be seen that the deformation heterogeneity was preferentially distributed near the grain boundary rather than within the crystal from the KAM analysis diagram in Fig. 12d. Therefore, cracking was more likely to occur at grain boundaries and interfaces due to local concentration of stress. Similar phenomenon had been reported by Rafi Ullah [50] when studying the microstructural evolution of laser additive manufacturing TC4. KAM values of $NiTi_2$ and NiTi two phase regions were statistically analyzed, as shown in Fig. 12e and f. The average KAM values of $NiTi_2$ and α-Ti region were 0.0232 and 0.0446, respectively. The Schmidt factor distribution diagram of $NiTi_2$ and α-Ti region was also investigated, as shown in Fig. 12g and h. The Schmidt factor played a dynamic role in material characterization which presented the shear stress applied to a particular slip system. As can be seen from Fig. 12g and h, the difference of Schmidt factor in the interface region was larger, which indicated that the plasticity at the interface was low [50].

Considering from the point of view of the actual component, the bending moment occurs when the component is subjected to wind resistance as the wing material. Therefore, the bending strength of the gradient heterogeneous alloy was characterized to make it more suitable for the stress state of the component. The bending curve of TC4/NiTi gradient heterogeneous alloy is shown in Fig. 13a. As can be seen from Fig. 13a, the sample was no yield stage, which was typical brittle fracture. The brittle fracture may be caused by the high content of hard phase near the interface of different gradient regions of the sample. In addition, the large difference of Schmidt factor distribution will also cause local stress concentration, thereby reducing the plasticity of materials. The maximum bending strength was 257.01 ± 26 MPa. Fig. 13b shows the bending fracture morphology. The overall fracture of the sample was relatively flat and smooth. High magnification image of bending fracture is shown in Fig. 13c, it can be seen from Fig. 13c that two types of typical regions had formed in the fracture. One fracture feature area was flat and smooth, with fluvial pattern and cleavage steps. The other was rough and mixed with fine broken particles, as shown in Fig. 13c. Therefore, it was reasonable to infer that the bending failure mechanism of the sample was consisted of transgranular fracture and intergranular brittle fracture.

In order to evaluate the mechanical properties of the TC4/NiTi gradient heterogeneous alloy, the sample was subjected to a compression test in which it was compressed until failure. The representative

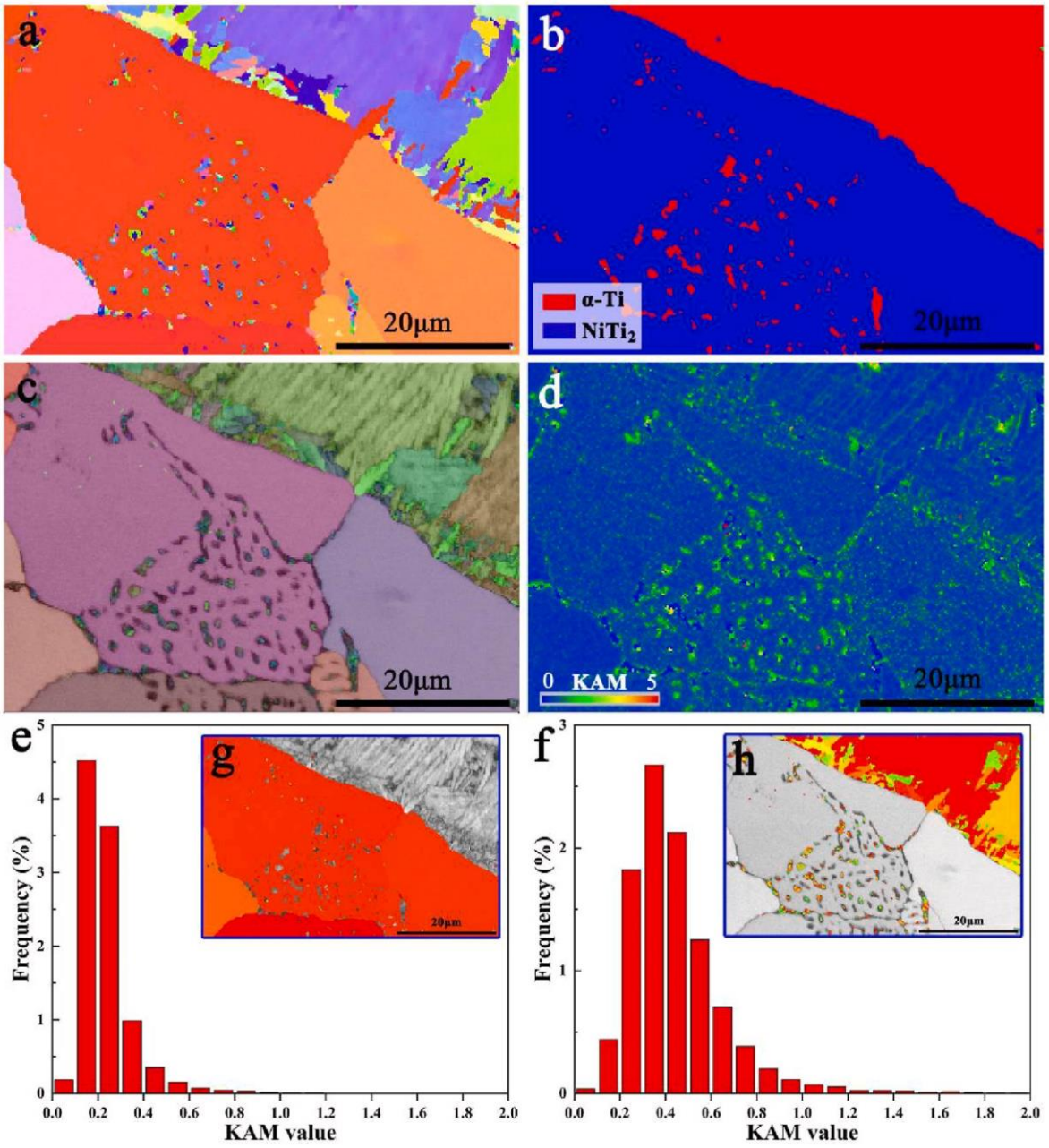

Fig. 12. EBSD results of interface I of MWAAM TC4/NiTi gradient heterogeneous alloy: (a) Grain morphology; (b) Phase distribution map; (c) BC map; (d) KAM map; (e–f) KAM value distribution maps; (g–h) Schmidt factor distribution maps; (e, g) $NiTi_2$ phase region; (f, h) α-Ti phase region.

stress-strain curves of lower region (TC4), middle region (TC4/NiTi) and upper region (NiTi) were shown in Fig. 14a. The fracture stress for three samples were 1638.54 ± 16 MPa, 1533.33 ± 26 MPa and 2222.93 ± 11 MPa, and the fracture strain were 36.0 ± 4%, 28.3 ± 6% and 31.2 ± 3%, respectively. The compression fracture morphology of sample is shown in Fig. 14b–d. It can be seen from Fig. 14b that there were irregular dimples region on the TC4 compression fracture surface, which was consistent with the highest plasticity of TC4 sample. In addition, a large number of fluvial patterns were observed in the fracture morphology of TC4 region. Therefore, the failure mechanism of TC4 sample was a mixed fracture of ductile fracture and brittle fracture. Interestingly, the compression curves of NiTi and TC4/NiTi gradient heterogeneous alloy samples were different from those of TC4 sample, as shown in Fig. 14a. The deformation of NiTi alloy experienced four main stages in compression test, the elastic deformation stage of austenite, the stress-induced martensitic transformation stage, the martensitic deformation stage, and the fracture stage [51]. The stress-strain curve of the NiTi sample reflected these four stages and indicated a fracture stress of 2222.93 ± 11 MPa with a corresponding fracture strain of 31.2%. The sample experienced an austenitic elastic deformation up to a strain of 3.0%, stress-induced martensite transformation between a strain of 3.0 (stress 212.56 MPa) and 13.01%, and martensitic deformation between a strain of 13.01% and 31.2%. In the martensitic deformation stage, martensite started to plastic deform and fractured at a strain of 18.19% with a corresponding fracture stress of 2222.93 ± 11 MPa. The shape of the TC4/NiTi gradient heterogeneous alloys sample compression curve was similar to that of the NiTi sample curve, and the typical four stages can also be observed in Fig. 14a. The component underwent austenitic elastic deformation at 2.85% strain, stress-induced martensitic transformation between 2.85 and 11% strain, and martensitic deformation between 11% and 15.33% strain. The corresponding martensitic deformation fracture stress was about 1533.33 ± 26 MPa. The fracture

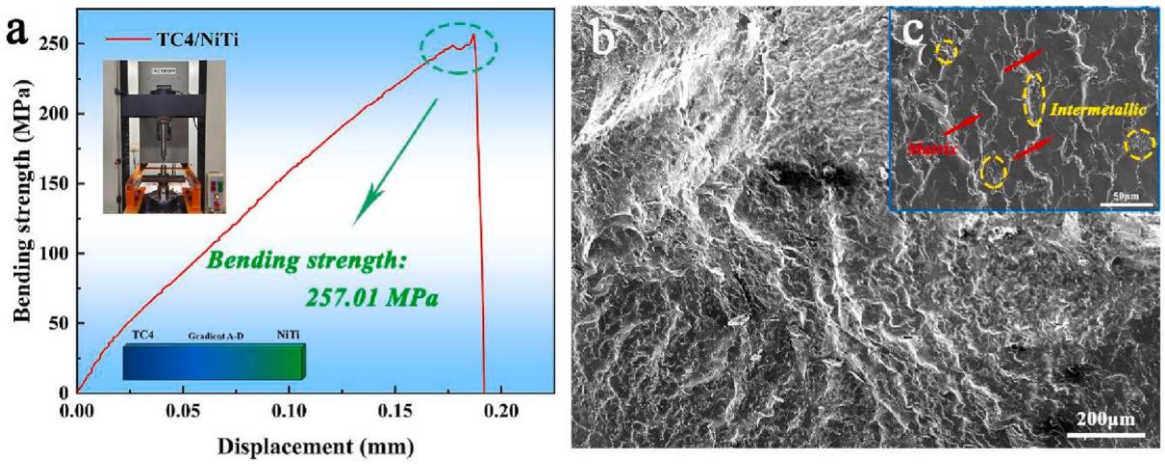

Fig. 13. Mechanical properties of MWAAM TC4/NiTi gradient heterogeneous alloy: (a) Typical load-displacement curves in bending tests; (b) SEM image of the fracture of the bending sample; (c) High magnification SEM image of fracture of the bending sample.

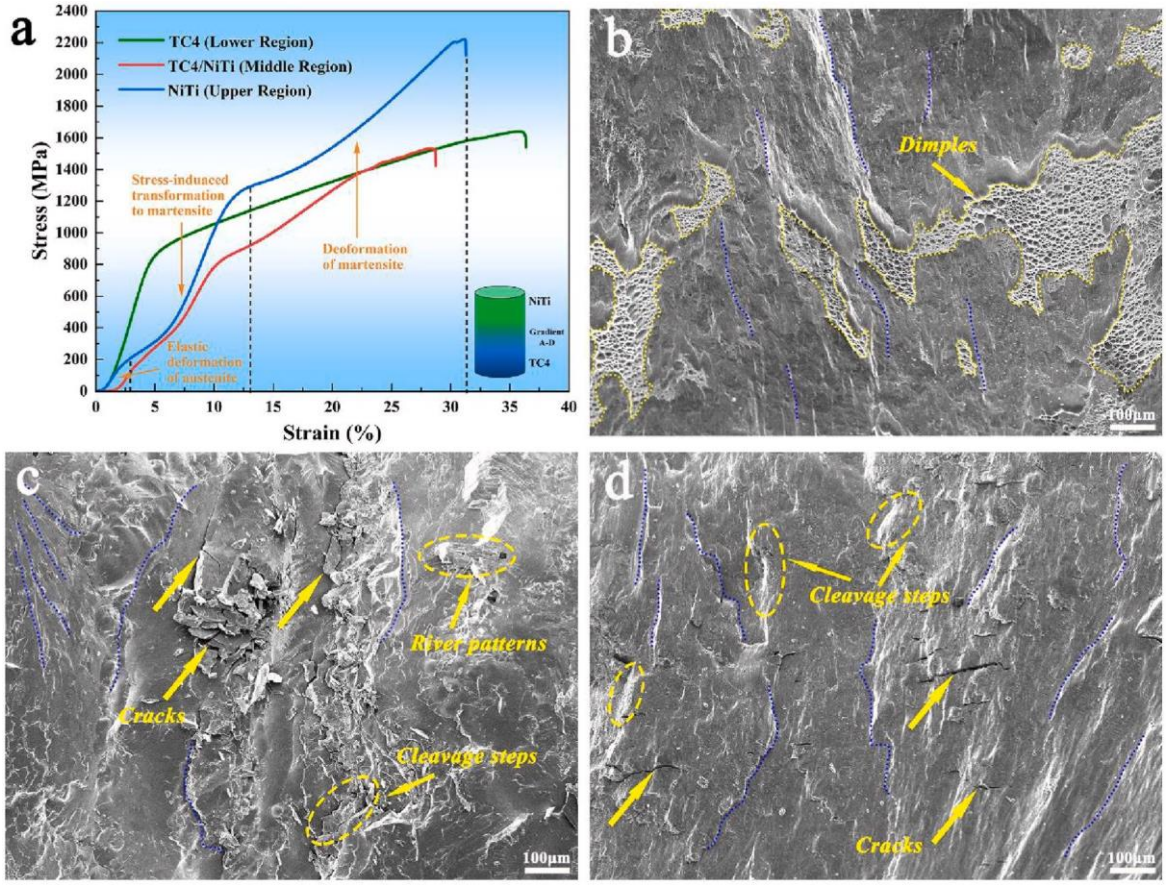

Fig. 14. Mechanical properties of MWAAM TC4/NiTi gradient heterogeneous alloy: (a) Stress-strain curves of different regions. SEM image of the fracture of the compressed sample: (b) TC4 region; (c) TC4/NiTi region; (d) NiTi region.

morphology of TC4/NiTi gradient heterogeneous alloy and NiTi samples was shown in Fig. 14c and d. Compared with Fig. 14d, there were more cleavages steps and cracks in Fig. 14c, indicating that the failure mechanism TC4/NiTi gradient heterogeneous alloy sample was mainly brittle fracture. The brittle fracture easily happened in the region where intermetallic compounds were concentrated [52]. According to the above analysis of the organization of the gradient region, there are different contents of $NiTi_2$ intermetallic compounds in the gradient region A-C. The large area accumulation $NiTi_2$ phase was easily to cause the stress concentration, resulting in it became the source of crack under the action of external forces. Once the crack was formed in the $NiTi_2$ phase aggregation zone, the bulk intermetallic compound phase will provide the preferred direction of crack propagation, and such zone (Such as region A and B) will accelerate the crack propagation. Since region C was composed of the network distribution of $NiTi_2$ and NiTi phases, the crack propagation in region C was usually accompanied by bifurcation, resulting in secondary cracks formed. The massive $NiTi_2$ phase will fracture during the process of brittle fracture, and the residual

$NiTi_2$ phase will be embedded in the fracture surface forming rough fragments, as shown in Fig. 14c. When the cracks propagating along $NiTi_2$ phase extend to a certain extent, transgranular fracture will occur, thus forming cleavage steps and river like patterns in the fracture surface. This phenomenon is more likely to happen in region C. Compared with NiTi samples, the strength and plasticity of TC4/NiTi gradient heterogeneous alloy samples were reduced. The main reasons for performance decrease are as follows: On the one hand, the number and area of $NiTi_2$ phase in the gradient sample were increased, which increased the stress concentration caused by the $NiTi_2$ phase aggregation. Meanwhile, the increase of the content of $NiTi_2$ phase increased the proportion of intergranular brittle fracture in the fracture mode and decreased the mechanical properties of the alloy [52]. On the other hand, the granular Ni_3Ti in NiTi alloy samples had a nailing effect on the crack growth, which helped to restrain the crack growth and improved the strength of the alloy. Based on the above analysis, it can be seen that the failure and fracture of TC4/NiTi gradient heterogeneous alloy mainly caused from gradient regions intermetallic compound of $NiTi_2$ in region A and B.

Cyclic compression tests were carried out on NiTi and TC4/NiTi gradient heterogeneous alloys to evaluate the superelasticity of the samples, and the results are shown in Fig. 15. During each compression test, a total of 10 loading/unloading cycles were tested at the same strain rate. The NiTi sample showed superelasticity deformation behavior, while the superelasticity characteristics were not obvious in the curves of TC4/NiTi gradient heterogeneous alloys during the loading-unloading process, as shown in Fig. 15a and **c**. The samples could not fully recover during the cyclic compression test due to that the cyclic compression test was performed at room temperature and the temperature did not exceed the final temperature of austenite transition [37]. The irrecoverable strain, recoverable strain and recovery ratio were calculated according to the curve in Fig. 15a and **c**, the results as shown in Fig. 15b and **d**. According to the statistical results in Fig. 15b, the recoverable strain in the first cycle was about 7.841%, and the corresponding recovery ratio is 78.41%. As the number of cycles increased, the recovery rate gradually decreased and remained at about 59.5% during the eighth load/unload cycle. The reason for the decrease of recovery rate was that the plastic deformation occurred during the stress induced martensitic transformation, as well as the continuous accumulated and slipped of dislocations during loading resulting in the failure to return to austenite during unloading [53–56]. Compared with the NiTi sample, the superelasticity of TC4/NiTi gradient heterogeneous alloy sample was relatively poor, as shown in Fig. 15d. In the 10 cycles of compression test, the recovery rate of TC4/NiTi gradient heterogeneous alloy was lower than 60%, and the highest recovery rate was 58.5% in the first cycle of loading-unloading process. In the tenth loading-unloading cycle, the recovery rate of TC4/NiTi gradient heterogeneous alloy sample was 54.18%, which was lower than the corresponding value of NiTi sample.

In NiTi based alloys, the size and morphology of grains, orientation texture, stress distribution, etc. have a significant impact on their superelasticity energy, especially the equiaxed grains are conducive to the response of superelasticity properties [57]. K. Otsuka et al. [58] believed that the region composed of coarse grains was more prone to deformation than that of fine grains, and unrecoverable changes were more likely to accumulate in the region of coarse grains. Compared with the coarse columnar grains, the fine grains can provide higher dislocation slip resistance, reduce the generation of microcracks in the process

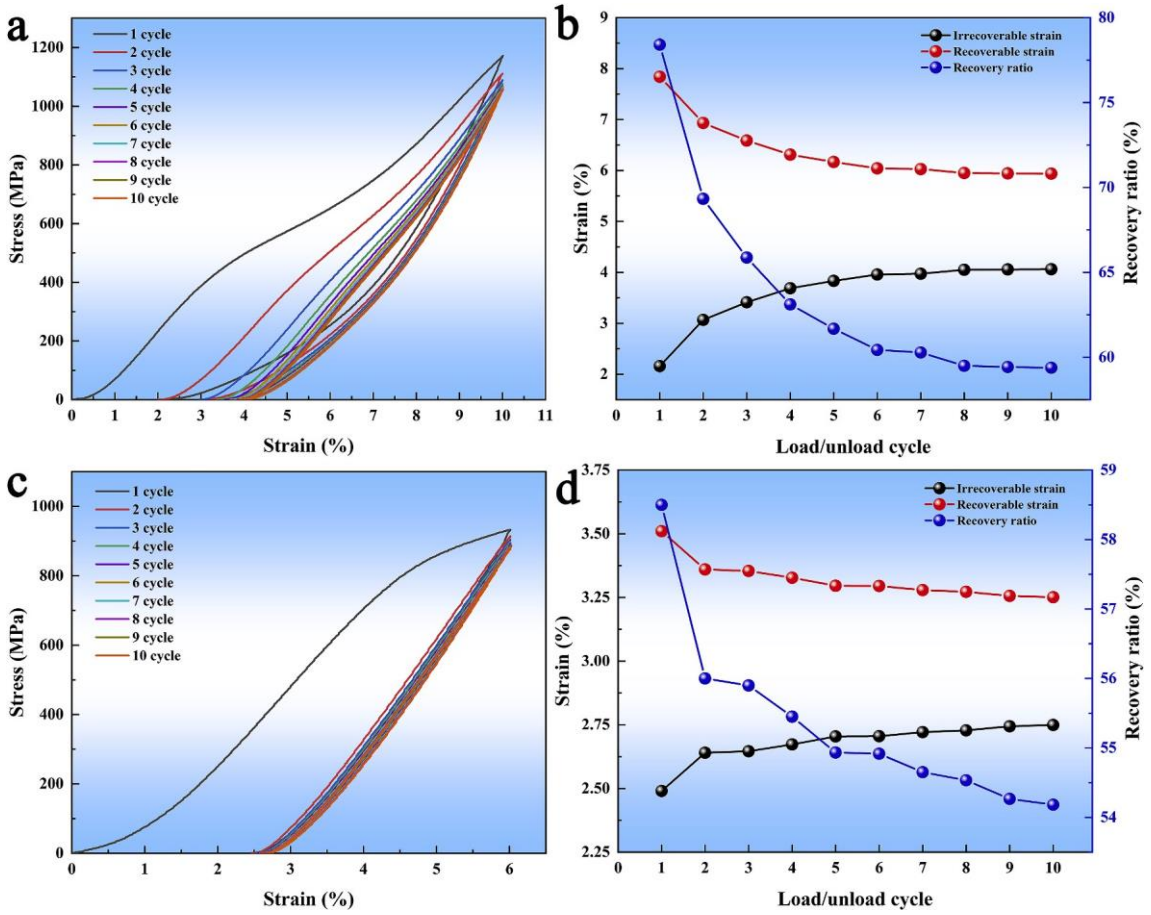

Fig. 15. Cyclic compression test of MWAAM NiTi and TC4/NiTi gradient heterogeneous alloy: (a, c) Cyclic stress-strain curves; (b, d) Transition of recoverable strain and irreversible strain and recovery ratio. (a–b) NiTi sample; (c–d) TC4/NiTi sample.

of martensite variant interface advancing, lead to less stress concentration and plastic deformation accumulation, and thus make the recoverable stress change larger. Li et al. [59] also considered that the coarse columnar grains in polycrystalline NiTi alloys have a delayed effect on the superelasticity reaction. Although the grains of gradient samples in the transition zone were mostly equiaxed, it should be noted that the precipitation of fine grain $NiTi_2$ irrelevant to the matrix had no effect on the improvement of superelasticity properties [60]. Therefore, the $NiTi_2$ phase of equiaxed crystal in the gradient sample will not bring gain effect to the superelasticity property of the sample. In addition, a number of other factors such as loading rate, sample surface treatment, and test environment can also affect the superelastic characteristics. In this paper, the microstructure evolution and mechanical properties test of TC4/NiTi alloy component manufactured by bionic gradient structure provided ideas for realizing the high strength connection of multi-material and multi-function heterogeneous alloys.

4. Conclusions

The TC4/NiTi gradient heterogeneous multi-materials structure thin-wall component was manufactured by multi-wire arc additive manufacturing. The microstructure and mechanical properties of component was investigated in detail. The results are summarized as follows.

(1) The microstructure evolution and element distribution of TC4/NiTi gradient heterogeneous alloy showed good metallurgical combination was obtained between different regions of the component. With an increase of the content NiTi, the phase of TC4/NiTi gradient heterogeneous alloy changed as follows: α-Ti+β-Ti→α-Ti + $NiTi_2$→$NiTi_2$→$NiTi_2$+NiTi→NiTi + Ni_3Ti.

(2) The gradient region of TC4/NiTi gradient heterogeneous alloy showed random orientation. The grain size was decreased from 3.389 μm to 2.047 μm from region A to region D. The polar density of gradient region A-D was significantly lower than TC4 and NiTi regions, indicating that the grain orientation of the gradient regions was more random. The Schmidt factor of MWAAM TC4/NiTi gradient heterogeneous alloy increased with increasing the content of NiTi, and the maximum average Schmidt factor appears in the NiTi region, reaching about 0.484.

(3) The microhardness of TC4/NiTi gradient heterogeneous alloy from TC4 to NiTi ranged from 310 ± 8 HV to 230 ± 11 HV. The region B exhibited highest hardness value was 669.6 ± 12 HV, which was due to the precipitation of $NiTi_2$ strengthening phase in region B. The plasticity of interface between TC4 and region A was low resulting from the local concentration of stress and large difference of Schmid factor.

(4) The maximum bending strength of TC4/NiTi gradient heterogeneous alloy was 257.01 ± 26 MPa. The bending failure mechanism of the sample was consisted of transgranular fracture and intergranular brittle fracture. The maximum compressive strength of TC4/NiTi sample was 1533.33 ± 26 MPa, which is 94% of that of TC4 sample (1638.54 ± 16 MPa) and 69% of that of NiTi sample (2222.93 ± 11 MPa). The superelasticity of MWAAM TC4/NiTi sample was lower than that of the NiTi sample, which was related to the $NiTi_2$ precipitated in the NiTi matrix and inhibited martensitic transformation. The recovery rate of TC4/NiTi gradient heterogeneous alloy sample was 54.18% after the tenth loading-unloading cycle. In this paper, MWAAM TC4/NiTi gradient heterogeneous metal multi-materials structure component were manufactured through bionic gradient structure, and it exhibited excellent mechanical properties.

CRediT authorship contribution statement

P.F. Jiang: Writing – original draft. **M.H. Nie:** Data curation. **X.M. Zong:** Formal analysis. **X.B. Wang:** Investigation. **Z.K. Chen:** Data curation. **C.Z. Liu:** Formal analysis. **J.Z. Teng:** Investigation. **Z.H. Zhang:** Validation.

Declaration of competing interest

The authors declare that they have no known competing financial interests or personal relationships that could have appeared to influence the work reported in this paper.

Data availability

No data was used for the research described in the article.

Acknowledgements

This work is supported by National Key Research and Development Program of China (Grant 2022YFB4600500) and the National Natural Science Foundation of China (Grant 52235006 and 52025053).

References

[1] L. Bhandari, V. Gaur, On study of process induced defects-based fatigue performance of additively manufactured Ti6Al4V alloy, Addit. Manuf. 60 (2022), 103227.
[2] S.L. Lu, Z.J. Zhang, R. Liu, X.H. Zhou, X.G. Wang, B.N. Zhang, X.M. Zhao, J. Eckert, Z.F. Zhang, Optimal tensile properties of laser powder bed fusion hereditary basket-weave microstructure in additive manufactured Ti6Al4V, Addit, Man 59 (2022), 103092.
[3] E. Iaparova, L. Heller, O. Tyc, P. Sittner, Thermally induced reorientation and plastic deformation of B19' monoclinic martensite in nanocrystalline NiTi wires, Acta Mater. 242 (2023), 118477.
[4] K.F. Xu, J. Luo, C. Li, Y.L. Shen, C.J. Li, X. Ma, M.Q. Li, Mechanisms of stress-induced martensitic transformation and transformation-induced plasticity in NiTi shape memory alloy related to superelastic stability, Scripta Mater. 217 (2022), 114775.
[5] S.H. Kim, H. Lee, S.M. Yeon, C.A. Jr, K. Choi, J. Yoon, S.W. Yang, H. Lee, Selective compositional range exclusion via directed energy deposition to produce a defect-free Inconel 718/SS 316L functionally graded material, Addit. Manuf. 47 (2021), 102288.
[6] T. Durejko, M. Zietala, W. Polkowski, T. Czujko, Thin wall tubes with Fe3Al/SS316L graded structure obtained by using laser engineered net shaping technology, Mater. Des. 63 (2014) 766–774.
[7] J.P. Oliveira, B. Panton, Z. Zeng, C.M. Andrei, Y. Zhou, R.M. Miranda, F.M. Braz Fernandes, Laser joining of NiTi to Ti6Al4V using a Niobium interlayer, Acta Mater. 105 (2016) 9–15.
[8] H.B. Deng, Y.H. Chen, Y.L. Jia, Y. Pang, T.M. Zhang, S.L. Wang, L.M. Yin, Microstructure and mechanical properties of dissimilar NiTi/Ti6Al4V joints via back-heating assisted friction stir welding, J. Manuf. Process. 64 (2021) 379–391.
[9] J.L. Xie, Y.H. Chen, L.M. Yin, T.M. Zhang, S.L. Wang, L.T. Wang, Microstructure and mechanical properties of ultrasonic spot welding TiNi/Ti6Al4V dissimilar materials using pure Al coating, J. Manuf. Process. 64 (2021) 473–480.
[10] H.H. Lee, H.K. Park, J. Jung, A. Amanov, H.S. Kim, Multi-layered gradient structure manufactured by single-roll angular-rolling and ultrasonic nanocrystalline surface modification, Scripta Mater. 186 (2020) 52–56.
[11] B.T. Wu, D.H. Ding, Z.X. Pan, D. Cuiuri, H.J. Li, J. Han, Z.Y. Fei, Effects of heat accumulation on the arc characteristics and metal transfer behavior in Wire Arc Additive Manufacturing of Ti6Al4V, J. Mater. Process. Technol. 250 (2017) 304–312.
[12] C.P. Xue, Y.X. Zhang, P.C. Mao, C.M. Liu, Y.L. Guo, F. Qian, C. Zhang, K.L. Liu, M. S. Zhang, S.Y. Tang, J.S. Wang, Improving mechanical properties of wire arc additively manufactured AA2196 Al-Li alloy by controlling solidification defects, Addit. Manuf. 43 (2021), 102019.
[13] T.Q. Xu, J.J. Huang, Y.A. Cui, C.C. Jing, T. Lu, S.Y. Ma, X. Ling, C.M. Liu, Exploring a novel panel-core connection method of large size lattice sandwich structure based on wire arc additive manufacturing, Mater. Des. 212 (2021), 110223.
[14] F. Bartolomeu, M.M. Costa, N. Alves, G. Miranda, F.S. Silva, Additive manufacturing of NiTi-Ti6Al4V multi-material cellular structures targeting orthopedic implants, Opt Laser. Eng. 134 (2020), 106208.
[15] C. Ciss´e, M.A. Zaeem, Design of NiTi-based shape memory microcomposites with enhanced elastocaloric performance by a fully thermomechanical coupled phase-field model, Mater. Des. 207 (2021), 109898.
[16] Y.J. Ren, J.G. Du, B. Liu, Z.B. Jiao, Y.T. Tian, I. Baker, H. Wu, Mater. Sci. Eng., A 848 (2022), 143402.

[17] R. Prasad, D.T. Waghmare, K. Kumar, M. Masanta, Effect of overlapping condition on large area NiTi layer deposited on Ti-6Al-4V alloy by TIG cladding technique, Surf. Coating. Technol. 385 (2020), 125417.
[18] Z.Q. Liu, M.A. Meyers, Z.F. Zhang, R.O. Ritchie, Functional gradients and heterogeneities in biological materials: design principles, functions, and bioinspired applications, Prog. Mater. Sci. 88 (2017) 467–498.
[19] Y. Politi, M. Priewasser, E. Pippel, P. Zaslansky, J. Hartmann, S. Siegel, C.H. Li, F. G. Barth, P. Fratzl, A Spider's Fang: How to design an injection needle using chitin-based composite material, Adv. Funct. Mater. 22 (2012) 2519–2528.
[20] J.C. Weaver, G.W. Milliron, A. Miserez, K. Evans-Lutterodt, S. Herrera, I. Gallana, W.J. Mershon, B. Swanson, P. Zavattieri, E. DiMasi, D. Kisailus, The stomatopod dactyl club: a formidable damage-tolerant biological hammer, Science 336 (2012) 1275–1280.
[21] V. Brul´e, A. Rafsanjani, M. Asgari, T.L. Western, D. Pasini, Three-dimensional functional gradients direct stem curling in the resurrection plant Selaginella lepidophylla, J. R. Soc. Interface 159 (16) (2019), 20190454.
[22] A. Miserez, T. Schneberk, C.J. Sun, F.W. Zok, J.H. Waite, The transition from stiff to compliant materials in squid beaks, Science 319 (2008) 1816.
[23] L. Ren, Z.G. Wang, L.Q. Ren, Z.W. Han, Q.P. Liu, Z.Y. Song, Graded biological materials and additive manufacturing technologies for producing bioinspired graded materials: an overview, Compos. B Eng. 242 (2022), 110086.
[24] P.F. Jiang, X.R. Li, X.M. Zong, X.B. Wang, Z.K. Chen, H.X. Yang, C.Z. Liu, N.K. Gao, Z.H. Zhang, Multi-wire arc additive manufacturing of Ti basic heterogeneous alloy: effect of deposition current on the microstructure, mechanical property and corrosion-resistance, J. Alloys Compd. 920 (2022), 166056.
[25] C. Wei, L.C. Liu, Y.C. Gu, Y.H. Huang, Q. Chen, Z.Q. Li, L. Li, Multi-material additive-manufacturing of tungsten - copper alloy bimetallic structure with a stainless-steel interlayer and associated bonding mechanisms, Addit. Manuf. 50 (2022), 102574.
[26] B.E. Carroll, R.A. Otis, J.P. Borgonia, J. Suh, R.P. Dillon, A.A. Shapiro, D. C. Hofmann, Z. Liu, A.M. Beese, Functionally graded material of 304L stainless steel and Inconel 625 fabricated by directed energy deposition: characterization and thermodynamic modeling, Acta Mater. 108 (2016) 46–54.
[27] R.X. Ma, Z.Q. Liu, W.B. Wang, G.J. Xu, W. Wang, Laser deposition melting of TC4/TiAl functionally graded material, Vacuum 177 (2020), 109349.
[28] J. Han, L.Z. Lu, Y. Xin, X.Y. Chen, G.Y. Zhang, Y.C. Cai, Y.B. Tian, Microstructure and mechanical properties of a novel functionally graded material from Ti6Al4V to Inconel 625 fabricated by dual wire + arc additive manufacturing, J. Alloys Compd. 903 (2022), 163981.
[29] G. Xu, L.J. Wu, Y.Y. Su, Z.F. Wang, K.Y. Luo, J.Z. Lu, Microstructure and mechanical properties of directed energy deposited 316L/Ti6Al4V functionally graded materials via constant/gradient power, Mater. Sci. Eng., A 839 (2022), 142870.
[30] H. Wang, S.Y. Ma, J.C. Wang, T. Lu, C.M. Liu, Microstructure and mechanical properties of TA15/TC11 graded structural material by wire arc additive manufacturing process, Trans. Nonferrous Metals Soc. China 31 (2021) 2323–2335.
[31] Y.H. Wang, S. Konovalov, X.Z. Chen, R.A. Singh, S. Jayalakshmi, Research on plasma arc additive manufacturing of Inconel 625 Ni-Cu functionally graded materials, Mater. Sci. Eng., A 853 (2022), 143796.
[32] C. Wei, L.C. Liu, H.T. Cao, X.L. Zhong, X. Xu, Y.C. Gu, D.X. Cheng, Y.H. Huang, Z. Q. Li, W. Guo, Z. Liu, L. Li, Cu10Sn to Ti6Al4V bonding mechanisms in laser-based powder bed fusion multiple material additive manufacturing with different build strategies, Addit. Manuf. 51 (2022), 102588.
[33] X. Tang, S. Zhang, X. Cui, C.H. Zhang, Y. Liu, J.B. Zhang, Tribological and cavitation erosion behaviors of nickel-based and iron-based coatings deposited on AISI 304 stainless steel by cold metal transfer, J. Mater. Res. Technol. 9 (3) (2020) 6665–6681.
[34] A.H.M.E. Rahman, M.N. Cavalli, Diffusion bonding of commercially pure Ni using Cu interlayer, Mater. Char. 69 (2012) 90–96.
[35] P.F. Jiang, X.R. Li, X.M. Zong, X.B. Wang, Z.K. Chen, C.Z. Liu, N.K. Gao, Z. H. Zhang, Microstructure and mechanical properties of Ti basic bionic gradient heterogeneous alloy prepared by multi-wire arc additive manufacturing, J. Alloys Compd. 926 (2022), 166813.
[36] W.E. Frazier, Metal additive manufacturing: a review, J. Mater. Eng. Perform. 23 (2014) 1917–1928.
[37] J. Han, X.Y. Chen, G.Y. Zhang, L.Z. Lu, Y. Xin, B. Liu, Y.C. Cai, X. Zhang, Y.B. Tian, Microstructure and mechanical properties of Ni50.8Ti49.2 and Ni53Ti47 alloys prepared in situ by wire-arc additive manufacturing, J. Mater. Process. Technol. 306 (2022), 117631.
[38] K. Otsuka, X. Ren, Physical metallurgy of Ti-Ni-based shape memory alloys, Prog. Mater. Sci. 50 (2005) 511–678.
[39] L. Yu, K.Y. Chen, Y.L. Zhang, J. Liu, L. Yang, Y.S. Shi, Microstructures and mechanical properties of NiTi shape memory alloys fabricated by wire arc additive manufacturing, J. Alloys Compd. 892 (2021), 162193.
[40] X. Cui, S. Zhang, Z.Y. Wang, C.H. Zhang, C.L. Ni, C.L. Wu, Microstructure and fatigue behavior of 24CrNiMo low alloy steel prepared by selective laser melting, Mater. Sci. Eng., A 845 (2022), 143215.
[41] J. Wang, Z.X. Pan, Y.F. Wang, L. Wang, L.H. Su, D. Cuiuri, Y.H. Zhao, H.J. Li, Evolution of crystallographic orientation, precipitation, phase transformation and mechanical properties realized by enhancing deposition current for dual-wire arc additive manufactured Ni-rich NiTi alloy, Addit. Manuf. 34 (2020), 101240.
[42] B.T. Wu, Z.X. Pan, D.H. Ding, D. Cuiuri, H.J. Li, Effects of heat accumulation on microstructure and mechanical properties of Ti6Al4V alloy deposited by wire arc additive manufacturing, Addit. Manuf. 23 (2018) 151–160.
[43] Y.C. Lin, Y. Tang, X.Y. Zhang, C. Chen, H. Yang, K.C. Zhou, Effects of solution temperature and cooling rate on microstructure and micro-hardness of a hot compressed Ti-6Al-4V alloy, Vacuum 159 (2019) 191–199.
[44] J.Q. Gong, K.W. Wei, M.N. Liu, W.J. Song, X.Y. Li, X.Y. Zeng, Microstructure and mechanical properties of AlSi10Mg alloy built by laser powder bed fusion/direct energy deposition hybrid laser additive manufacturing, Addit. Manuf. 59 (2022), 103160.
[45] P.F. Jiang, C.H. Zhang, S. Zhang, J.B. Zhang, J. Chen, H.T. Chen, Additive manufacturing of novel ferritic stainless steel by selective laser melting: role of laser scanning speed on the formability, microstructure and properties, Opt Laser. Technol. 140 (2021), 107055.
[46] P.F. Jiang, C.H. Zhang, S. Zhang, J.B. Zhang, J. Chen, Y. Liu, Microstructure evolution, wear behavior, and corrosion performance of alloy steel gradient material fabricated by direct laser deposition, J. Mater. Res. Technol. 9 (5) (2020) 11702–11716.
[47] X.H. Zhan, Q. Wang, L.L. Wang, Z.N. Gao, X.Y. Yang, Regionalization of microstructure and mechanical properties of Ti6Al4V transition area fabricated by WAAM-LMD hybrid additive manufacturing, J. Alloy, Compd 929 (2022), 167345.
[48] X. Cui, S. Zhang, C. Wang, C.H. Zhang, J. Chen, J.B. Zhang, Effects of stress-relief heat treatment on the microstructure and fatigue property of a laser additive manufactured 12CrNi2 low alloy steel, Mater. Sci. Eng., A 791 (2020), 139738.
[49] X. Wang, C.H. Zhang, X. Cui, S. Zhang, J. Chen, J.B. Zhang, Novel gradient alloy steel with quasi-continuous ratios fabricated by SLM: material microstructure and wear mechanism, Mater. Char. 174 (2021), 111020.
[50] R. Ullah, J.X. Lu, L.J. Sang, M. Rizwan, Y.F. Zhang, Z. Zhang, Investigating the microstructural evolution during deformation of laser additive manufactured Ti-6Al-4V at 400 ◦C using in-situ EBSD, Mater. Sci. Eng., A 823 (2021), 141761.
[51] Y. Liu, Z. Xie, J.V. Humbeeck, L. Delaey, Asymmetry of stress ± strain curves under tension and compression for NiTi shape memory alloys, Acta Mater. 46 (12) (1998) 4325–4338.
[52] D.J. Wu, C.C. Song, T.D. Di, F.Y. Niu, G.Y. Ma, Intermetallic regulation mechanism of Inconel 718/Ti6Al4V composite by novel follow-up ultrasonic assisted laser additive manufacturing, Compos. B Eng. 235 (2022), 109736.
[53] M. Elahinia, N.S. Moghaddam, M.T. Andani, A. Amerinatanzi, B.A. Bimber, R. F. Hamilton, Fabrication of NiTi through additive manufacturing: a review, Prog. Mater. Sci. 83 (2016) 630–663.
[54] J.P. Oliveira, R.M. Miranda, N. Schell, F.M.B. Fernandes, High strain and long duration cycling behavior of laser welded NiTi sheets, Int. J. Fatig. 83 (2016) 195–200.
[55] H.Z. Lu, C. Yang, X. Luo, H.W. Ma, B. Song, Y.Y. Li, L.C. Zhang, Ultrahigh-performance TiNi shape memory alloy by 4D printing, Mater. Sci. Eng., A 763 (2019), 138166.
[56] J.P. Oliveira, F.M.B. Fernandes, N. Schell, R.M. Miranda, Martensite stabilization during superelastic cycling of laser welded NiTi plates, Mater. Lett. 171 (2016) 273–276.
[57] N. Li, S.A. Huang, G.D. Zhang, R.Y. Qin, W. Liu, H.P. Xiong, G.Q. Shi, J. Blackburn, Progress in additive manufacturing on new materials: a review, J. Mater. Sci. Technol. 35 (2019) 242–269.
[58] K. Otsuka, X. Ren, Physical metallurgy of Ti-Ni-based shape memory alloys, Prog. Mater. Sci. 50 (2005) 511–678.
[59] B.Q. Li, L. Wang, B.B. Wang, D.H. Li, R. Cui, B.X. Su, L.H. Yao, L.S. Luo, R. Chen, Y. Q. Su, J.J. Guo, H.Z. Fu, Solidification characterization and its correlation with the mechanical properties and functional response of NiTi shape memory alloy manufactured by electron beam freeform fabrication, Addit. Manuf. 48 (2021), 102468.
[60] Q. Zhou, M.D. Hayat, G. Chen, S. Cai, X.H. Qua, H.P. Tang, P. Cao, Selective electron beam melting of NiTi: microstructure, phase transformation and mechanical properties, Mater. Sci. Eng., A 744 (2019) 290–298.